The Astrophysical Journal, 819:123 (23pp), 2016 March 10 doi:10.3847/0004-637X/819/2/123

STAR FORMATION BLACK HOLE GROWTH AND DUSTY TORI IN THE MOST LUMINOUS AGNS AT $Z = 2$–3.5

Hagai Netzer[1], Caterina Lani[1], Raanan Nordon[1], Benny Trakhtenbrot[2,5], Paulina Lira[3], and Ohad Shemmer[4]
[1] School of Physics and Astronomy and the Wise Observatory, The Raymond and Beverly Sackler Faculty of Exact Sciences, Tel-Aviv University, Tel-Aviv 69978, Israel; netzer@wise.tau.ac.il
[2] Institute for Astronomy, Department of Physics, ETH Zurich, Wolfgang-Pauli-Strasse 27, CH-8093 Zurich, Switzerland
[3] Departamento de Astronomia, Universidad de Chile, Camino del Observatorio 1515, Santiago, Chile
[4] Department of Physics, University of North Texas, Denton, TX 76203, USA
Received 2015 July 2; accepted 2016 January 20; published 2016 March 7

ABSTRACT

We report *Herschel*/SPIRE observations of 100 very luminous, optically selected active galactic nuclei (AGNs) at $z = 2$–3.5 with $\log L_{1350}$ (erg s^{-1}) $\geqslant 46.5$, where L_{1350} is λL_{λ} at 1350 Å. The distribution in L_{1350} is similar to the general distribution of Sloan Digital Sky Survey AGNs in this redshift and luminosity interval. We measured star-formation (SF) luminosity, $L_{\rm SF}$, and SF rate (SFR) in 34 detected sources by fitting combined SF and torus templates, where the torus emission is based on *Wide Field Infrared Survey Explorer* observations. We also obtained statistically significant stacks for the undetected sources in two luminosity groups. The sample properties are compared with those of very luminous AGNs at $z > 4.5$. The main findings are: (1) The mean and the median SFRs of the detected sources are 1176^{+476}_{-339} and 1010^{+706}_{-503} $M_{\odot}$ yr^{-1}, respectively. The mean SFR of the undetected sources is 148 $M_{\odot}$ yr^{-1}. The ratio of SFR to the black hole accretion rate is ≈80 for the detected sources and less than 10 for the undetected sources. Unlike a sample of sources at $z \simeq 4.8$ that we studied recently, there is no difference in $L_{\rm AGN}$ and only a very small difference in $L_{\rm torus}$ between the detected and undetected sources. (2) The redshift distribution of $L_{\rm SF}$ and $L_{\rm AGN}$ for the most luminous, redshift 2–7 AGNs are different. Similar to previous studies, the highest $L_{\rm AGN}$ are found at $z \approx 3$. However, the $L_{\rm SF}$ of such sources peaks at $z \approx 5$. Assuming the objects in our sample are hosted by the most massive galaxies at those redshifts, we find that approximately 2/3 of the hosts are already below the main sequence of SF galaxies at $z = 2-3.5$. (3) The spectral energy distributions (SEDs) of dusty tori at high redshift are similar to the shapes found in low redshift, low luminosity AGNs. *Herschel* upper limits put strong constraints on the long wavelength shape of the SED, ruling out several earlier suggested torus templates as applicable for this sample. (4) We find no evidence for a luminosity dependence of the torus covering factor in sources with $\log L_{\rm AGN}$ (erg s^{-1}) $= 44-47.5$. This conclusion is based on the recognition that the estimated $L_{\rm AGN}$ in several earlier studies is highly uncertain and non-uniformally treated. The median covering factors over this range are 0.68 for isotropic dust emission and 0.4 for anisotropic emission.

Key words: galaxies: active – galaxies: star formation – quasars: general

1. INTRODUCTION

The comparison of black hole (BH) growth and star formation (SF) across cosmic time is essential for understanding the parallel evolution of galaxies and super-massive BHs. This topic has received much attention during the last decade, in particular since the launch of ESA Herschel Space Observatory (Pilbratt et al. 2010; hereafter *Herschel*). This mission provided superb far-infrared (FIR) capability and a deeper, more systematic study of SF rate (SFR), specific SFR (sSFR), and SF luminosity ($L_{\rm SF}$) at high redshift. It is now possible to compare $L_{\rm SF}$ and active galactic nucleus (AGN) bolometric luminosity ($L_{\rm AGN}$) over a large redshift range in thousands of sources at $z < 1$ and hundreds of sources at $z > 2$. At $z \sim 1$, *Herschel*/PACS, with bands at 70, 100, and 160 μm, provides the most reliable FIR fluxes, and thus $L_{\rm SF}$, for the host galaxies of AGNs with $L_{\rm AGN} \geqslant 10^{45}$ erg s^{-1}. For $z > 2$, *Herschel*/SPIRE (Griffin et al. 2010), with bands at 250, 350, and 500 μm, is more efficient and detection is limited only by confusion noise, which translates to $\log L_{\rm SF}$ (erg s^{-1}) ~ 45.6 erg s^{-1} ($\sim$100 $M_{\odot}$ yr^{-1}) at $z = 2 - 3$.

Studies of AGN hosts show that at all redshifts most AGNs reside in SF galaxies (e.g., Silverman et al. 2008; Mainieri et al. 2011; Mullaney et al. 2012; Rosario et al. 2012; Santini et al. 2012). Moreover, there is no evidence for different host properties between systems with active or dormant BHs that have the same stellar mass (M_*; Rosario et al. 2013). There is already extensive literature on the comparison of $L_{\rm SF}$ and $L_{\rm AGN}$ at all redshifts, with somewhat ambiguous conclusions (e.g., Netzer 2009; Hatziminaoglou et al. 2010; Shao et al. 2010; Harrison et al. 2012; Mullaney et al. 2012; Page et al. 2012; Rosario et al. 2012; Chen et al. 2013; Hickox et al. 2014; Stanley et al. 2015 and references therein). Some of the differences depend on the selection method: FIR is basically SF selection, whereas X-ray is preferentially AGN selection. It also depends on the treatment of undetected objects (stacking, statistical analysis of upper limits, etc.), which are usually the majority of the sources at high redshift. A general result that emerged from these studies is that the $L_{\rm SF}$–$L_{\rm AGN}$ plane can be divided into two regimes with very different distributions. The first is the "SF-dominated" regime, where $L_{\rm SF} > L_{\rm AGN}$. Here the correlation between $L_{\rm SF}$ and $L_{\rm AGN}$ depends critically on the selection and averaging methods. In studies like Rosario et al. (2012) and Stanley et al. (2015), selection and binning is by X-ray flux and stacking by FIR flux. In this case, there is no apparent correlation between $L_{\rm SF}$ and $L_{\rm AGN}$. In contrast, FIR selected samples (Mullaney et al. 2012; Chen et al. 2013; Delvecchio et al. 2015) where binning is in FIR flux and

[5] Zwicky postdoctoral fellow.

stacking is by X-ray flux show a clear correlation between log ($L_{\rm SF}$) and log($L_{\rm AGN}$) with a slope very close to unity. In the second "AGN-dominated" regime, where $L_{\rm AGN} > L_{\rm SF}$, the sources seem to cluster around a power-law line of the form $L_{\rm SF} \propto L_{\rm AGN}{}^{0.7}$. There are a few theoretical attempts to explain these correlations based on the different duration of SFR and BH accretion (Neistein & Netzer 2014), the different duty cycles (Hickox et al. 2014), and the nature of SF and BH accretion in merging galaxies (Thacker et al. 2014; Volonteri et al. 2015a, 2015b).

This work is a continuation of Netzer et al. (2014), which discusses $L_{\rm AGN}$ and $L_{\rm SF}$ in a flux-limited sample of optically selected $z \simeq 4.8$ AGNs. These objects are the most luminous AGNs powered by the most massive BHs at this redshift. Out of the 44 AGNs in that sample, 10 were detected by *Herschel*/SPIRE and stacking of 29 undetected sources gave statistically significant fluxes at all SPIRE bands. Five more sources gave ambiguous results. Netzer et al. (2014) compared $L_{\rm SF}$, $L_{\rm AGN}$, and BH mass ($M_{\rm BH}$) in the detected and undetected source, and showed that the detected sources with the higher $L_{\rm SF}$ are also those with the higher $L_{\rm AGN}$ and more massive BHs. The *Herschel*-detected sources are located close to the border between the two aforementioned regimes with $L_{\rm AGN} \sim L_{\rm SF}$. The related work of Leipski et al. (2014) provided similar data for a large number of luminous, randomly selected AGNs at $z > 5$. In their study the detection limit is very high, due to the high redshift. As a result, the number of directly detected sources is less than 10 and there is no statistically meaningful way to compare $L_{\rm SF}$, $L_{\rm AGN}$, and BH mass.

The present work follows our earlier study of high redshift, luminous AGNs. It presents data on the most luminous type-I AGNs at $z = 2$–3.5 observed by *Herschel* using deep SPIRE observations. This means that we avoid several studies of very high luminosity type-II AGNs like the Castignani & De Zotti (2015) and Drouart et al. (2014) works on radio-loud sources. We focus on two central themes of AGN research. The first is SF in the host galaxies of these sources, and the second is the near-Infrared (NIR) and mid-infrared (MIR) dust emission in the vicinity of the central BHs. The latter is related to AGN tori; a topic that has been studied extensively since the mid-1980s (see Antonucci 1993 for review of the earlier results and ideas, and the recent review by Netzer 2015 where newer developments and more recent references are provided). One way to study such tori is to compare the observed NIR–MIR luminosity, $L_{\rm torus}$, with $L_{\rm AGN}$ and derive the "torus covering factor" as a function of source luminosity. This covering factor is directly related to the fraction of type-I and type-II AGNs at different redshifts (e.g., Treister et al. 2008; Lusso et al. 2013; Roseboom et al. 2013; Merloni et al. 2014, and references therein). Here we extend these studies to the highest possible luminosity and focus on the spectral energy distribution (SED) emitted by the torus, the anisotropy of the torus radiation, and the way to determine the covering factor.

The structure of the paper is as follows. In Section 2 we describe the sample and the Wide Field Infrared Survey Explorer (*WISE*) and *Herschel* data. Section 3 provides a detailed explanation of the method used to separate SF and torus emission in *Herschel*-detected and undetected sources. We use our new data and those from the literature to discuss SF and AGN emission at $z > 2$, and to provide new information about the torus emission and covering factor at all luminosities and redshifts. Section 4 presents the conclusions of our work.

Throughout this paper we assume $H_0 = 70\ {\rm km\,s^{-1}\,Mpc^{-1}}$, $\Omega_M = 0.3$, and $\Omega_\Lambda = 0.7$. For the conversion to SFR we assume that $L_{\rm SF}$ is obtained from integration over the 8–1000 μm range, and $1 M_\odot\,{\rm yr}^{-1}$ corresponds to a slightly rounded value of $10^{10}\,L_\odot$ based on a Chabrier initial mass function (Chabrier 2003) as adopted by Nordon et al. (2012).

2. SAMPLE SELECTION OBSERVATIONS AND DATA ANALYSIS

2.1. Sample Selection

The sample selected for this study consists of type-I AGNs found in data-release 7 (DR7) of the Sloan Digital Sky Survey (SDSS; Abazajian et al. 2009) and observed by *Herschel*/SPIRE (see Griffin et al. 2010). The chosen redshift range is 2–3.5 and the chosen luminosity is $\log \lambda L_\lambda(1350\ \text{Å}\ {\rm erg\ s^{-1}}) \geqslant 46.5$ (hereafter L_{1350}). *Herschel* observed 16 objects of the entire sample as part of a dedicated open-time cycle 2 project (PI: H. Netzer). Five of these sources are not SDSS AGN. The remainder are obtained from the *Herschel* archive; this includes targeted and serendipitous sources, as well as objects in several large GTO surveys. We used the Shen et al. (2011) catalog that lists all bright AGNs with SDSS spectra, and searched the *Herschel* archive for sources that exceed the chosen L_{1350} in that catalog (3383 sources) and were observed by *Herschel*. The search includes AGNs observed with SPIRE in a "Small Scan" mode and sources that are located in relatively large fields observed by various key projects. We searched for such sources in the following extragalactic fields: H-ATLAS (Eales et al. 2010), COSMOS (Scoville et al. 2007), Extended Groth Strip (EGS; Davis et al. 2007), ELAIS (Rowan-Robinson et al. 1999), Lockman Hole (Lonsdale et al. 2003), Strip-82 (Adelman-McCarthy et al. 2007), and Böotes (Jannuzi et al. 2004). This list does not cover every field observed with SPIRE and reflects the publicly available *Herschel* data that was correct to late 2014. For these fields we use the catalogs, publicly released images, and the standard pipeline. The total number of sources identified in this way is about 120. Only a handful of the selected sources were observed by *Herschel*/PACS. The small number is not sufficient for stacking analysis, and we decided not to use these observations because their inclusion will affect the uniformity of the sample in an undesirable way. We only consider observations where the SPIRE confusion limits have been reached. With SPIRE resolution, the 1σ flux limits correspond roughly to 5.8 mJy at 250 μm, 6.3 mJy at 350 μm, and 6.8 mJy at 500 μm. Some candidates were located behind lensing clusters. We decided not to include lensed sources due to the complications associated with the lensing.

Of the originally selected sources, we decided to remove about 20. One source was removed because of a neighboring source less than 5 arc-sec away. All other sources that were removed from the original list were not detected by *Herschel* and are situated very close to the edge of their field or in other areas with large gaps in the *Herschel* scans. There are clear indications that the confusion limits have not been reached in these cases. The total number of *Herschel*-observed sources that remained after this procedure is 100. Out of these, 34 are considered detections with 3σ flux detection in 3 (31 sources) or 2 (250 and 350 μm, 3 sources) of the SPIRE bands. The rest have upper limits in all three bands (see Section 2.2). Given the relatively large range in torus luminosity that affects the

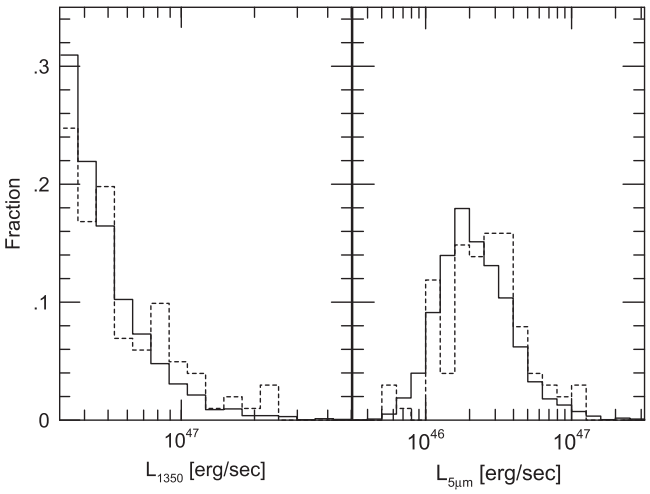

Figure 1. Left: a comparison of the bolometric luminosity distribution of the *Herschel*-observed AGNs with log $L_{\rm bol}$ (erg s^{-1}) $\geqslant$ 46.5 and z = 2–3.5 (dashed line) with the distribution of all SDSS AGNs from Shen et al. (2011) in the same luminosity and redshift range (solid line). Right: the same for $L_{5\mu m}$.

measurements of $L_{\rm SF}$ (Section 2.3), we divided the sources into two subgroups based on their L_{1350}. The first group consists of objects with 46.5 $\leqslant$ log L_{1350} (erg s^{-1}) $\leqslant$ 46.7 and the second 46.7 $<$ log L_{1350} (erg s^{-1}). There are 57 (19 detected and 38 upper limits) AGNs in the former group and 43 (15 detected and 28 upper limits) in the latter group.

The *Herschel* observations are part of several different observing programs, which have different goals and are not covering the SDSS part of the sky in a systematic way. We therefore checked how representative of the general population these sources are by comparing the luminosity distribution of our 100 AGNs with all type-I AGNs from the Shen et al. (2011) catalog covering the same L_{1350} and redshift range. The comparison is shown in Figure 1. We tested the null hypothesis that the two distributions are drawn from the same parent population using the standard, two-distribution KS test. The resulting probability, $p = 0.071$, suggests that the null hypothesis cannot be ruled out. We also compared the redshift distributions of the two samples across the chosen range of 2–3.5. The distributions are very similar, with an almost identical median and a KS probability of $p = 0.93$. After separating into luminosity groups, we find a median redshift of 2.57 for the low luminosity group and 2.50 for the high luminosity group.

2.2. Herschel Flux Measurements

The fluxes in the small scan SPIRE maps were measured using the *sourceExtractorSussextractor* task in the *Herschel* software package HIPE (for details of the algorithm and parameters see Savage & Oliver 2007). This task extracts the fluxes for all sources detected in the image simultaneously, and thus also partially solves for confusion/blending with nearby sources. In the first iteration, the task was run as a blind extraction on the 250 μm image, with the detection threshold set to 3 σ plus the target's optical coordinates as priors. If no source was found within 5″ from the optical prior location, a second iteration was run using the source list from the first iteration. The flux extraction from the 350 and 500 μm images used the coordinates of the blindly detected 250 μm sources as priors. For all our sources, there were no cases of 350 μm blind detections without 250 μm counterparts. The 500 μm images are much more affected by confusion and a list of priors is always necessary for their extraction. In the large fields of major SPIRE projects (H-ATLAS SDP, described in Pascale et al. 2011 and Rigby et al. 2011; HerS, described in Viero et al. 2014; HerMES, Oliver et al. 2012) we take the fluxes provided in the source catalogs as released by the corresponding teams, using a "3–5" search radius around the SDSS coordinates.

2.3. Stacking of Non-detected Herschel Sources

The majority of our *Herschel*-observed sources (68%) was not detected in any of the SPIRE bands. In such cases, we used a stacking analysis that was done separately for the two luminosity subgroups. The stacking procedure is identical to that used by Nordon et al. (2012) and has been thoroughly tested in previous works. It is based on many previous works in the literature, such as Béthermin et al. (2010) and Dole et al. (2006). In the present work, we obtained both mean and median stacks for the two luminosity groups.

The depth of the SPIRE fields is usually limited by confusion due to multiple/bright nearby sources, rather than by instrument noise. The SPIRE confusion limits are approximately 5.8, 6.3, and 6.8 mJy at 250, 350, and 500 μm, respectively (Nguyen et al. 2010). Stacking the images on the (optically measured) position of otherwise undetected sources reduces the confusion by roughly (0.5–1)$\sqrt{N}$ and increases the accuracy of the mean (or median) flux accordingly. For stacking, we use *residual images* that were created by removing all sources detected by sourceExtractorSussextractor (using the standard tools within the HIPE package). This procedure does not remove any flux from the (undetected) stacked sources and serves only to somewhat flatten the background. Working on residual images makes it easier to determine the background level and lowers some of the confusion noise in the final stacked image. Residual images were constructed for all fields used in this work. The images must use the same pixel scale; therefore, we reprojected those images with different scales onto a new grid. The background level is determined by creating a histogram of pixel fluxes and locating its peak. The removal of the bright sources from the residual image contributed to removing the high values tail in the histogram, making the distribution more symmetric around its peak. The peak of the distribution represents the most likely background flux value of a randomly chosen pixel. This flux is subtracted from the image before stacking (i.e., the new pixel-flux histogram is centered on zero).

For each stacking position, we project the residual image onto a small grid ("stamp") with the optical source coordinates centered on the central pixel. The stamps are collected into a cube, where each stamp is multiplied by the redshift correction factor (see Section 2.3.1). We then take the mean (or median) value of a cube column (same pixel in all stamps) as the value for the corresponding pixel in the stacked image. Thus, the final stacked images represent the mean or median fluxes for our sample. We also create background stacks, where we stack on random locations in the residual images, selected to be at least several PSFs away from the location of the optical source. The number of background stamps is four times the number of stacked sources, but from this pool of stamps each bootstrap step (see Section 2.4) draws a number of stamps similar to that of the real sources stacks. By duplicating in parallel every step

done with the real sources stack, the background stacks serve as a control and an estimator of the noise level (instrumental and confusion), as well as of biases due to inaccuracies in background subtraction.

The flux in a final mean or median stacked image is measured from the peak of a fitted 2D Gaussian to the source in the center of the image with a sub-pixel allowance for adjustments in peak location and FWHM. These minor adjustments are necessary because the stamps are taken from different *Herschel* images, which may potentially have slightly different systematic offsets in coordinates relative to the optical positions. The flux in the background stacked image is measured in an identical way and is used as an estimator to the systematic error due to the non-zero background (verified to be smaller than the random errors by factor of a few) and the significance of detection (see Section 2.4). The median stacks that were used in this work are shown in Figure 10.

2.3.1. Redshift and K-corrections

Our stacking analysis requires mixing fluxes from different redshifts, so we need to assign an effective redshift to the stacked source. If we were comparing a sample of detected sources, we would apply a redshift *k*-correction to each source to account for the different rest-frame wavelengths of the SPIRE bands, and a correction due to the different luminosity distances. For the stacks, we apply the same procedure (all redshifts are known), but do so to each stamp in the cube before taking the means or the medians. This was done assuming a stacked redshift of $z = 2.5$, which is very close to the median redshifts listed above. For the redshift range chosen (2–3.5), the *k*-correction and the luminosity distance correction tend to cancel each other out, and the combined factor is very close to 1 (0.85–1.35 with a median of 1.1 for the 250 μm stacks and an even narrower range for the longer wavelength stacks).

For the *k*-correction, we use a warm ULIRG template ($\log(L_{\rm IR}/L_{\odot}) > 12.7$) from the Chary & Elbaz (2001) library (the exact template shape makes only a little difference). This translates to

$$k = \frac{F_{\nu}(\lambda_{\rm filter}/(1+2.5))}{F_{\nu}(\lambda_{\rm filter}/(1+z))}, \quad (1)$$

where F_{ν} is the template flux as a function of rest-frame frequency and $\lambda_{\rm filter}$ is the observed wavelength of the band. We note that the slope of this template at wavelengths longer than the FIR peak is quite close to the slope of the Mor & Netzer (2012) torus SEDs (a topic that is discussed in detail in Section 3.4). Thus, for most combinations of SPIRE filters and source redshifts in our sample, there is little difference whether we assume a (relatively) warm SF dust emission, or a pure torus emission. In any combination of wavelength and redshift (the worst being at $z = 3.5$), the difference between using a torus template and a ULIRG template for the *k*-correction is less than 10%, and in most cases it is much lower around the median redshift of 2.5. As for the luminosity distance, we corrected the fluxes to $D_{\rm L}(z = 2.5)$.

2.4. Bootstrap Uncertainties

We use a standard bootstrap method to estimate the uncertainty on the stacked fluxes of our sources. From our cube of N stamps, we randomly resample N stamps allowing repetition. In parallel we select N stamps from the background stamp cube. The new cubes are then treated in the exact same way as the originals and a mean or median flux is measured. The process is repeated 500 times to obtain a distribution of resampled fluxes. The central 68% of the distribution was taken as the $\pm 1\sigma$ limits on the measured medians. The limits represent a combination of noise and the intrinsic spread of source fluxes within the sample. The corresponding lower and upper limits obtained from the background stack are used to estimate the significance of detection of the stacked source (i.e., ruling out the null hypothesis that the stacked source is a fluctuation: a combination of instrumental and confusion noise).

2.5. WISE Measurements and Torus SED

All our sources were detected by *WISE* (Wright et al. 2010) in at lease one of its four bands: 3.4 (W1), 4.6 (W2), 12 (W3), and 22 (W4) μm. General discussions of the most luminous *WISE*-detected AGNs are given in Weedman et al. (2012) and Vardanyan et al. (2014), which include all the sources in our sample. These references also detail the standard data extraction procedure we use in the present work. For the chosen redshift range, the four bands cover the rest-frame 1–7 μm wavelength range and are employed to determine the torus SED and covering factor.

The torus SED template we use throughout this paper is the one suggested by Mor & Netzer (2012). This SED is based on fitting *Spitzer* spectra, after subtracting an SF contribution, and NIR photometry of approximately 100 nearby, type-I AGNs. The data were fitted with a three-component model: a hot (~1400–1800 K) dust source, assumed to represent the inner walls of the torus where only graphite grains can survive the local flux of the central source; a warm graphite+silicate torus based on the calculations of Nenkova et al. (2008b); and dust emission from the NLR. This template was extended to the FIR by combining it with a 100 K, $\beta = 1.5$ gray body at $\lambda > 35$ μm. The SED is roughly flat, in λL_{λ}, between 2 and 25 μm, and then drops sharply at longer wavelengths. Mor & Netzer (2012) discussed the uncertainty of the shape of the SED and its dependence on source luminosity (see their Figure 6). The study of *WISE*/SDSS AGNs by Vardanyan et al. (2014) shows that the very flat SED between 2 and 10 μm is a common property of the most luminous AGNs at high redshift.

An earlier paper by Mullaney et al. (2011) proposed somewhat different, luminosity-dependent SEDs, turning down at longer wavelengths in the range of 30–40 μm. The work is based on fitting broken power-law models to MIR-FIR data after subtracting the SF contribution. The main differences between the two works are the different assumptions about the SF contribution to the observed MIR emission, which in turn can influence the derived SED shape at long wavelengths, the assumed clumpy torus versus a broken power law, and the treatment of the very hot dust. As shown in Section 2.5, some of the Mullaney et al. (2011) SEDs seem to be in conflict with our *Herschel* observations. A different torus model proposed by Polletta et al. (2006) and Polletta et al. (2007), was used by Tsai et al. (2015) to study extremely luminous high-redshift AGNs and compare them with the most luminous galaxies discovered by *WISE*. The 2–20 μm part of this SED is in good agreement with the Mor & Netzer (2012) template, but its long wavelength part is very different and is also in conflict with our *Herschel* observations as discussed in Section 2.5.

A large part of the difference must be due to the neglect of SF contribution to the long wavelength part of this template that was assumed to be AGN-dominated.

Several recent works (Assef et al. 2013; Lira et al. 2013; Lusso et al. 2013; Roseboom et al. 2013; Leipski et al. 2014) adopted different fitting methods. Roseboom et al. (2013) used various combinations of a hot blackbody and a warm dusty torus to fit broad-band NIR–MIR data in a large sample of *WISE*-selected sources. Lusso et al. (2013) used broad-band JHK and *Spitzer* MIR data to fit 513 XMM-COSMOS sources. Their assumed torus SED is more empirical, based on observations of low luminosity AGNs. The approach adopted by Leipski et al. (2014) is similar to the Roseboom et al. (2013) method. Finally, Lira et al. (2013) fitted local type-II AGNs with several different theoretical predictions.

The NIR emission of dusty tori in type-I AGN can vary considerably from one source to the next. The variation is stronger than that observed in the MIR part, with some 10%–20% of the sources showing much weaker 2–4 μm dust emission. Such objects, here referred to as "weak-NIR" AGNs, have been investigated in detail in several papers (e.g., Mor & Trakhtenbrot 2011; Mor & Netzer 2012; Roseboom et al. 2013; Leipski et al. 2014). The SED adopted here is inappropriate for the weak-NIR sources.

The prescription from our preferred torus model (see Section 3.4) corresponds to $L_{\rm torus} = (3.58^{+0.69}_{-0.4})\ L_{5\mu{\rm m}}$, where $L_{5\mu{\rm m}}$ stands for λL_λ at 5 μm, $L_{\rm torus}$ is the observed integrated SED over the 1–200 μm range, and the upper and lower limits are the values corresponding to the 25 and 75 percentiles in Mor & Netzer (2012). As explained in Section 3.4, this is a very good assumption for all the objects in our sample, except for the weak-NIR sources (12 objects). Obviously, the total energy radiated by the torus can differ substantially from $L_{\rm torus}$, due to anisotropic dust emission (Section 3.4.3).

To complete the comparison with the general population at $2 \leqslant z \leqslant 3.5$, we used the entire SDSS sample from the Shen et al. (2011) catalog, with the above mentioned redshift and luminosity cuts, and obtained *WISE* data for all these sources. We calculated the luminosities in the W3 (12 μm) and W4 (22 μm) windows, and used them to estimate $L_{5\mu{\rm m}}$. We only consider sources with 3σ detections in the W1, W2, and W3 bands (3217 objects out of the total of 3383). For sources with both W3 and W4 3σ detections (72% of the cases), we used a linear interpolation in $\log(L)$ to estimate $L_{5\mu{\rm m}}$. For the remaining sources, with upper limits on the flux in W4, we assume that $L_{5\mu{\rm m}}$ equals the W3 luminosity. Given the very similar luminosities in the W3 and W4 bands (which we verified for all sources with detections in both bands), this is a very good approximation of $L_{5\mu{\rm m}}$ given our choice of the torus SED. The results of the comparison are shown as two histograms in Figure 1. The histograms look similar and the probability of the two-distribution KS test is $p = 0.035$. More information about the luminosity distribution of the SDSS AGNs observed by *WISE* is given in Vardanyan et al. (2014).

Table 1 provides basic information about the sample and Table 2 lists the newly obtained fluxes and luminosities. The median and the mean stack fluxes are given in Table 3.

2.6. L_{AGN} Estimates: Bolometric Correction Factors

Two of the central issues discussed in this paper—the correlation between $L_{\rm AGN}$ and $L_{\rm SF}$, and that between $L_{\rm AGN}$ and $L_{\rm torus}$—depend on the method used to estimate $L_{\rm AGN}$. This requires the use of bolometric correction factors applied to the observed continuum luminosity at different wavelengths. The bolometric correction factor was a point of some confusion in earlier studies and, hence, requires more explanation (e.g., Marconi et al. 2004; Richards et al. 2006; Runnoe et al. 2012a, 2012b; Trakhtenbrot & Netzer 2012; Krawczyk et al. 2013). Because L_{1350} is directly probing the AGN accretion power, we use this wavelength to estimate $L_{\rm AGN}$.

The work of Marconi et al. (2004) suggests that all bolometric correction factors, at all wavelengths, decrease with increasing $L_{\rm AGN}$. This general trend was confirmed in later works, but the actual factors are rather different. For example, at the very high luminosity end ($\log L_{1350}$ (erg s^{-1}) $\sim$47), the bolometric correction factor suggested by Shen et al. (2011) for L_{1350} is 3.8, it is ~2 for Trakhtenbrot & Netzer (2012), ~3.23 for Runnoe et al. (2012a), and less than 2 for Krawczyk et al. (2013; extrapolating from their calculations at 2500Å). All numbers quoted here refer to isotropic emission at all wavelengths. As shown in Section 3, these differences can considerably affect some of the conclusions about AGN tori. Runnoe et al. (2012b) gives a systematic study of the bolometric correction factors in the range 1.5–24 μm. The numbers at 3 and 7 μm are basically identical and can be translated to the wavelength of interest here (5 μm) as a bolometric correction factor of approximately 8.5 ± 0.8. This gives $L_{5\mu{\rm m}}/L_{1350} \simeq 0.38$ for $\log L_{1350}$ (erg s^{-1}) $= 47$. In our sample the median value is $L_{5\mu{\rm m}}/L_{1350} \simeq 0.44$ with a 25–75 percentile range of 0.36–0.55. Thus, at the high luminosity end our numbers and those of Runnoe et al. (2012b) are in very good agreement.

The approach we adopt here is to use the same bolometric correction factor for all our high luminosity sources. Our bolometric correction factors are taken from Trakhtenbrot & Netzer (2012) and are based on a large sample of SDSS AGNs and the inter-calibration of continuum luminosities at three wavelength bands: 5100, 3000, and 1400 Å. The scaling is a combination of the luminosity-dependent correction factors suggested by Marconi et al. (2004), which were checked and verified over a large range of luminosity and redshift. Of particular importance in high-redshift objects is $\rm Bol_{1350}$, the bolometric correction factor applied to L_{1350}. Trakhtenbrot & Netzer (2012) show that for high luminosity AGNs, $\rm Bol_{1350} \sim 2$ with a rather large scatter, the order a factor 2 (but note that only 230 sources from the large sample were available for analysis). This estimate is independent of L_{1350}, therefore we also experimented with a second approximation, $\rm Bol_{1350} = 49 - L_{1350}$, which gives bolometric correction factors between 2.5 and 1.6 in the present sample and is also consistent with the results of Trakhtenbrot & Netzer (2012). The bolometric correction factor is in somewhat better agreement with thin accretion disk models of (e.g., Capellupo et al. 2015). As shown in Section 3.4.3, such differences can lead to different conclusions concerning the estimates of the torus covering factor.

2.7. Combined Torus and Star Formation SEDs

At the redshifts considered here, the three SPIRE bands cover roughly the rest-frame 50–170 μm. This wavelength range is the region where the torus emission drops rapidly toward longer wavelength and where the SF emission should peak. The FIR luminosity of many of our sources is considerably below their NIR–MIR luminosity, but the torus

Table 1
The $z = 2$–3.5 Sample: Positions, Redshifts, UV and AGN Luminosities

ID	R.A. (deg)	Decl. (deg)	z	$\log L_{1350}$ (erg s^{-1})	$\log L_{\rm AGN}$ (erg s^{-1})	*Scan ID*
SDSS J002025.22+154054.7	5.1051	15.6819	2.0087	46.84	47.14	1342213198
SDSS J005202.40+010129.2	13.0100	1.0248	2.2706	47.02	47.32	1342201380
SDSS J005229.51−110309.9	13.1230	−11.0528	2.4524	46.50	46.81	1342199390
SDSS J005814.31+011530.2	14.5597	1.2584	2.4949	46.90	47.20	HerS
SDSS J010227.51+005136.8	15.6146	0.8602	2.5319	46.66	46.97	HerS
SDSS J010612.21+001920.1	16.5509	0.3223	3.1196	46.71	47.01	HerS
SDSS J011552.59+000601.0	18.9691	0.1003	3.1933	46.52	46.82	HerS
SDSS J011827.99−005239.8	19.6166	−0.8777	2.1861	46.60	46.90	HerS
SDSS J012412.46−010049.8	21.0520	−1.0138	2.8300	46.98	47.29	HerS
SDSS J012517.14−001828.9	21.3214	−0.3080	2.2780	46.59	46.89	HerS
SDSS J012748.31−001333.0	21.9513	−0.2259	2.0748	46.56	46.86	HerS
SDSS J013014.30−000639.2	22.5596	−0.1109	2.3847	46.69	46.99	HerS
SDSS J013249.38+002627.1	23.2058	0.4409	3.1664	46.65	46.96	HerS
SDSS J013654.33−003415.4	24.2264	−0.5710	2.7317	46.56	46.87	HerS
SDSS J014123.04−002422.0	25.3460	−0.4061	2.5979	46.63	46.93	HerS
SDSS J014214.75+002324.2	25.5615	0.3901	3.3704	47.00	47.30	HerS
SDSS J014303.16+001039.6	25.7632	0.1777	2.5066	46.56	46.86	HerS
SDSS J014733.58+000323.2	26.8899	0.0565	2.0400	46.53	46.84	HerS
SDSS J014809.64−001017.8	27.0402	−0.1716	2.1627	46.69	46.99	HerS
SDSS J015017.71+002902.4	27.5738	0.4840	2.9774	46.53	46.83	HerS
SDSS J015819.77−001222.0	29.5824	−0.2061	3.3017	46.69	46.99	HerS
SDSS J015925.07−001755.4	29.8545	−0.2987	3.2570	46.72	47.02	HerS
SDSS J020719.65−001959.8	31.8319	−0.3333	3.4013	46.80	47.11	HerS
SDSS J020948.58+002726.6	32.4524	0.4574	2.6929	46.69	46.99	HerS
SDSS J020950.71−000506.4	32.4613	−0.0851	2.8282	47.33	47.63	HerS
SDSS J021724.53−010357.5	34.3522	−1.0660	2.2345	46.51	46.81	HerS
SDSS J022205.54+004335.2	35.5231	0.7265	2.5259	46.50	46.80	HerS
HE 0251−5550	43.1672	−55.6422	2.3505	47.27	47.57	1342270329
SDSS J031712.23−075850.3	49.3010	−7.9807	2.6957	46.59	46.90	1342239839
SDSS J075547.83+220450.1	118.9493	22.0806	2.3210	46.92	47.22	1342270319
SDSS J081127.44+461812.9	122.8644	46.3036	2.2592	47.16	47.46	1342270275
SDSS J081940.58+082357.9	124.9191	8.3994	3.2147	46.67	46.97	1342270311
SDSS J082138.94+121729.9	125.4123	12.2917	3.1128	46.56	46.86	1342254515
SDSS J083249.39+155408.6	128.2058	15.9024	2.4165	46.55	46.85	1342270302
SDSS J084846.10+611234.6	132.1921	61.2096	2.2558	47.20	47.50	1342270242
SDSS J085417.61+532735.2	133.5734	53.4598	2.4182	46.92	47.23	1342270247
SDSS J085825.71+005006.7	134.6071	0.8352	2.8550	46.56	46.87	H−ATLAS SDP
SDSS J085856.00+015219.4	134.7334	1.8721	2.1566	46.82	47.12	H−ATLAS SDP
SDSS J085959.14+020519.7	134.9964	2.0888	2.9804	46.88	47.18	H−ATLAS SDP
SDSS J090444.33+233354.0	136.1847	23.5650	2.2570	46.93	47.23	1342270297
SDSS J091054.79+023704.5	137.7283	2.6179	3.2951	46.75	47.05	H−ATLAS SDP
SDSS J091247.59−004717.3	138.1983	−0.7882	2.8593	46.55	46.86	H−ATLAS SDP
SDSS J092024.44+662656.7	140.1019	66.4491	2.0187	46.62	46.92	1342229122
SDSS J092325.25+453222.2	140.8552	45.5395	3.4524	47.07	47.37	1342270256
SDSS J092849.24+504930.5	142.2052	50.8252	2.3488	46.64	46.94	1342230874
SDSS J095112.84+025527.3	147.8035	2.9242	2.3732	46.52	46.83	1342209294
SDSS J095434.93+091519.6	148.6456	9.2554	3.3817	46.69	46.99	1342197310
SDSS J100515.99+480533.3	151.3166	48.0926	2.3850	47.01	47.31	1342270254
SDSS J101120.39+031244.5	152.8350	3.2124	2.4580	46.93	47.23	1342198868
SDSS J102325.31+514251.0	155.8555	51.7142	3.4510	47.18	47.48	1342270253
SDSS J102719.13+584114.3	156.8297	58.6873	2.0248	46.54	46.84	1342245910
SDSS J104018.51+572448.1	160.0772	57.4134	3.4089	46.88	47.18	Lockman-North
SDSS J104121.88+563001.2	160.3412	56.5003	2.0519	46.61	46.91	Lockman-Swire
SDSS J104442.15+381257.2	161.1756	38.2159	2.0745	46.57	46.87	1342254049
SDSS J104639.43+584047.7	161.6643	58.6799	3.1801	46.73	47.03	Lockman-North
SDSS J104809.19+570241.9	162.0383	57.0450	3.2487	46.77	47.08	Lockman-North
SDSS J105146.05+592214.0	162.9419	59.3706	2.9040	46.57	46.87	Lockman-Swire
SDSS J105902.04+580848.6	164.7585	58.1469	2.2444	46.69	46.99	Lockman-Swire
SDSS J110445.39+573643.9	166.1892	57.6122	2.6419	46.54	46.84	Lockman-Swire
SDSS J111313.29+102212.4	168.3054	10.3701	2.2475	46.72	47.02	1342199324
SDSS J111928.37+130251.0	169.8682	13.0475	2.3940	46.68	46.98	1342198883
SDSS J113157.72+191527.7	172.9905	19.2577	2.9153	46.80	47.10	1342256846
SDSS J113627.81+541504.4	174.1159	54.2512	3.2360	46.61	46.92	1342195958

Table 1
(Continued)

ID	R.A. (deg)	Decl. (deg)	z	$\log L_{1350}$ (erg s^{-1})	$\log L_{\rm AGN}$ (erg s^{-1})	*Scan ID*
SDSS J114412.76+315800.8	176.0532	31.9669	3.2350	46.76	47.06	1342256832
SDSS J115517.34+634622.0	178.8223	63.7728	2.8882	46.86	47.16	1342256631
SDSS J122307.52+103448.1	185.7813	10.5801	2.7422	46.58	46.89	1342234890
SDSS J122654.39−005430.6	186.7266	−0.9085	2.6170	46.66	46.97	1342234883
SDSS J123132.37+013814.0	187.8849	1.6373	3.2286	46.77	47.08	1342257370
SDSS J123515.83+630113.3	188.8160	63.0204	2.3885	46.93	47.23	1342270217
SDSS J123637.45+615814.3	189.1560	61.9707	2.5199	46.55	46.85	GOODS-North
SDSS J123714.60+064759.5	189.3108	6.7999	2.7811	46.54	46.84	1342234888
SDSS J123743.08+630144.8	189.4295	63.0291	3.4250	46.62	46.92	1342256809
SDSS J124302.42+521009.8	190.7601	52.1694	2.5588	46.51	46.81	1342198244
SDSS J124456.98+620143.0	191.2374	62.0286	3.0569	46.66	46.97	1342256811
SDSS J124748.44+042627.1	191.9519	4.4409	2.7833	46.58	46.88	1342189442
SDSS J125125.36+412000.4	192.8557	41.3335	3.1734	46.60	46.90	1342188754
SDSS J125819.24+165717.6	194.5802	16.9549	2.7015	46.64	46.94	1342259439
SDSS J131215.22+423900.8	198.0635	42.6502	2.5668	46.62	46.92	1342248486
SDSS J132809.59+545452.7	202.0400	54.9147	2.0958	46.81	47.12	1342256892
SDSS J133219.65+622715.9	203.0819	62.4544	3.1783	46.52	46.83	1342256897
SDSS J133907.13+131039.6	204.7797	13.1777	2.2411	46.65	46.95	1342259446
SDSS J135559.03−002413.6	208.9960	−0.4038	2.3366	46.59	46.89	1342202220
SDSS J141819.22+044135.0	214.5801	4.6931	2.5006	46.79	47.09	1342213465
SDSS J142539.01+331009.5	216.4125	33.1693	2.3056	46.58	46.88	Boötes
SDSS J142539.98+344843.5	216.4166	34.8121	2.2516	46.54	46.84	Boötes
SDSS J142912.87+340959.0	217.3037	34.1664	2.2289	46.66	46.97	Boötes
SDSS J143543.71+342906.4	218.9322	34.4851	2.5731	46.68	46.98	Boötes
SDSS J143941.92+332519.5	219.9247	33.4221	2.2536	46.54	46.84	Boötes
SDSS J143954.64+334658.9	219.9777	33.7831	3.4390	46.63	46.93	Boötes
SDSS J145706.34+220548.6	224.2764	22.0969	3.1114	46.52	46.82	1342201450
SDSS J155744.01+330231.0	239.4334	33.0420	3.1380	46.88	47.18	1342229549
SDSS J161238.26+532255.0	243.1594	53.3820	2.1392	46.76	47.07	ELAIS
SDSS J210831.56−063022.5	317.1315	−6.5063	2.3447	47.07	47.38	1342270337
SDSS J212329.46−005052.9	320.8728	−0.8480	2.2614	47.37	47.67	1342270338
LBQS 2154−2005	329.2747	−19.8538	2.0350	46.68	46.98	1342270203
HE 2156−4020	329.9779	−40.0972	2.5310	47.02	47.32	1342270330
2QZ J221814.4−300306	334.5603	−30.0517	2.3836	46.69	46.99	1342270331
2QZ J222006.7−280324	335.0279	−28.0564	2.4060	47.37	47.67	1342270332
SDSS J222256.11−094636.2	335.7338	−9.7767	2.9264	46.91	47.22	1342219976
SDSS J233446.40−090812.2	353.6933	−9.1367	3.3169	47.09	47.39	1342234748

Note. R.A., decl., and UV luminosities are taken from Shen et al. (2011); $L_{\rm AGN}$ was obtained as described in Section 3.1.

contribution at FIR energies must be taken into account properly in order not to be confused with the SF emission. We take this into account by fitting both the *WISE* and SPIRE photometry using a composite SED that includes a torus and SF components. We first fit the torus template to the *WISE* data using the rest-frame fluxes between 1.5–6 μm. We do not take into account systematic changes in the shape of the torus, partly because there is no spectroscopic information about the spectral shape at high luminosity and partly because our own analysis appears to justify the chosen SED at $\lambda > 25\,\mu$m (see Section 3.4). We fit the template to the data using a simple sum-of-squares minimization. The logarithmic uncertainty on the scaling of the template is determined from

$$\sigma^2_{\rm scale} = \frac{t^2}{N(N-1)} \sum_{\rm filter} (\log \nu L_\nu({\rm filter}) - \log \nu L_\nu({\rm template}))^2, \quad (2)$$

where t is the student t-test correction factor required to correct the standard deviation estimate to represent 68% when the number of points (N) is small. In almost all cases, the uncertainties on the torus luminosities are very small. Note that these are formal errors based on the assumption of an identical torus SED for all sources. Even small changes in the SED, like those described in Mor & Netzer (2012), will result in additional scatter that can be significantly larger than the scaling uncertainties used here.

Once the SED scaling is determined, we subtract the torus contribution from the flux in the SPIRE bands and add (in quadrature) the torus scaling uncertainty to the SPIRE photometric errors. The torus-subtracted fluxes are then fitted with an SF galaxy template from the Chary & Elbaz (2001) SED library. The fit allows some flexibility in both dust temperature (template shape) and scaling (total IR luminosity) by considering all the templates in the library whose 250/(1 + z) μm luminosity is in the range of $\pm$0.5 dex from the observed value. In all cases, PAH contributions to the W4 *WISE* band are extremely small, of order 1%, and hence do not affect the pre-determined torus SED. We then minimize χ^2 in the SPIRE bands and select the template with the lowest value. We prefer this method to the one involving all five bands because the χ^2 values in the W3 and W4 bands are significantly

Table 2
The $z = 2-3.5$ Sample: *WISE* and *Herschel* Fluxes and Luminosities Derived from SED Fittings

ID	$F_{3.4\mu m}$ (mJy)	$F_{4.6\mu m}$ (mJy)	$F_{12\mu m}$ (mJy)	$F_{22\mu m}$ (mJy)	$F_{250\mu m}$[a] (mJy)	$F_{350\mu m}$[a] (mJy)	$F_{500\mu m}$[a] (mJy)	$\log L_{5\mu m}$ (erg s^{-1})	$\log L_{SF}$ $L_{\odot}$
SDSS J002025.22+154054.7	0.76 ± 0.02	1.07 ± 0.03	2.50 ± 0.17	3.28 ± 1.17	0.00	0.00	0.00	46.31 ± 0.05	…
SDSS J005202.40+010129.2	0.54 ± 0.02	0.77 ± 0.03	2.49 ± 0.27	6.06 ± 1.68	0.00	0.00	0.00	46.46 ± 0.13	…
SDSS J005229.51−110309.9	0.22 ± 0.01	0.33 ± 0.02	1.70 ± 0.13	2.74 ± 1.07	43.38 ± 2.60	41.13 ± 2.63	31.18 ± 3.27	46.28 ± 0.04	$13.03^{+0.01}_{-0.01}$
SDSS J005814.31+011530.2	0.35 ± 0.01	0.52 ± 0.02	2.63 ± 0.20	6.96 ± 1.20	0.00	0.00	0.00	46.60 ± 0.16	…
SDSS J010227.51+005136.8	0.18 ± 0.01	0.30 ± 0.02	1.41 ± 0.17	3.96 ± 1.40	0.00	0.00	0.00	46.35 ± 0.18	…
SDSS J010612.21+001920.1	0.19 ± 0.01	0.21 ± 0.01	1.16 ± 0.17	4.12 ± 1.11	0.00	0.00	0.00	46.54 ± 0.26	…
SDSS J011552.59+000601.0	0.09 ± 0.01	0.11 ± 0.01	0.63 ± 0.27	3.10 ± 1.70	0.00	0.00	0.00	46.37 ± 0.39[b]	…
SDSS J011827.99−005239.8	0.31 ± 0.01	0.53 ± 0.02	2.42 ± 0.14	5.82 ± 1.14	37.86 ± 6.60	22.50 ± 6.15	23.12 ± 8.38	46.40 ± 0.13	$12.88^{+0.06}_{-0.07}$
SDSS J012412.46−010049.8	1.25 ± 0.03	1.34 ± 0.03	3.47 ± 0.15	7.76 ± 1.02	0.00	0.00	0.00	46.81 ± 0.08	…
SDSS J012517.14−001828.9	0.24 ± 0.01	0.30 ± 0.01	1.00 ± 0.19	2.16 ± 1.14	0.00	0.00	0.00	46.03 ± 0.09	…
SDSS J012748.31−001333.0	0.46 ± 0.01	1.01 ± 0.03	6.08 ± 0.16	19.91 ± 1.08	65.49 ± 5.97	24.57 ± 6.32	12.60 ± 7.68	46.82 ± 0.25[b]	$13.01^{+0.04}_{-0.04}$
SDSS J013014.30−000639.2	0.23 ± 0.01	0.37 ± 0.02	1.92 ± 0.13	2.42 ± 0.92	0.00	0.00	0.00	46.25 ± 0.13	…
SDSS J013249.38+002627.1	0.14 ± 0.01	0.17 ± 0.01	0.53 ± 0.15	2.92[c]	0.00	0.00	0.00	46.07 ± 0.18	…
SDSS J013654.33−003415.4	0.13 ± 0.01	0.16 ± 0.01	0.46 ± 0.13	3.59[c]	35.16 ± 7.56	19.27 ± 7.97	18.70 ± 9.31	45.85 ± 0.17	$13.01^{+0.07}_{-0.09}$
SDSS J014123.04−002422.0	0.30 ± 0.01	0.30 ± 0.01	0.62 ± 0.17	2.22 ± 1.34	0.00	0.00	0.00	46.07 ± 0.27	…
SDSS J014214.75+002324.2	0.32 ± 0.01	0.28 ± 0.01	0.97 ± 0.12	4.04[c]	0.00	0.00	0.00	46.57 ± 0.32	…
SDSS J014303.16+001039.6	0.25 ± 0.01	0.31 ± 0.01	1.68 ± 0.17	3.90 ± 1.16	0.00	0.00	0.00	46.37 ± 0.11	…
SDSS J014733.58+000323.2	0.42 ± 0.01	0.70 ± 0.02	2.72 ± 0.16	6.23 ± 0.94	0.00	0.00	0.00	46.33 ± 0.14	…
SDSS J014809.64−001017.8	0.36 ± 0.01	0.65 ± 0.02	2.76 ± 0.12	7.00 ± 0.84	81.65 ± 7.47	73.49 ± 7.56	76.10 ± 9.12	46.45 ± 0.15	$13.23^{+0.02}_{-0.02}$
SDSS J015017.71+002902.4	0.12 ± 0.01	0.20 ± 0.01	1.44 ± 0.11	2.83 ± 1.01	66.22 ± 6.21	83.78 ± 6.43	60.77 ± 7.58	46.45 ± 0.03	$13.43^{+0.02}_{-0.02}$
SDSS J015819.77−001222.0	0.18 ± 0.01	0.21 ± 0.01	1.36 ± 0.11	4.37 ± 0.87	40.66 ± 7.70	25.93 ± 8.01	9.13 ± 9.22	46.65 ± 0.22	$13.08^{+0.08}_{-0.09}$
SDSS J015925.07−001755.4	0.14 ± 0.01	0.16 ± 0.01	1.05 ± 0.12	2.07 ± 0.90	0.00	0.00	0.00	46.41 ± 0.03	…
SDSS J020719.65−001959.8	0.25 ± 0.01	0.22 ± 0.01	0.44 ± 0.12	3.18[c]	0.00	0.00	0.00	46.36 ± 0.53	…
SDSS J020948.58+002726.6	0.21 ± 0.01	0.29 ± 0.01	1.87 ± 0.12	6.05 ± 1.06	0.00	0.00	0.00	46.57 ± 0.23	…
SDSS J020950.71−000506.4	0.92 ± 0.02	1.33 ± 0.03	5.63 ± 0.17	15.40 ± 0.95	75.47 ± 10.91	64.20 ± 10.43	41.81 ± 11.48	47.07 ± 0.16	$13.24^{+0.11}_{-0.15}$
SDSS J021724.53−010357.5	0.15 ± 0.01	0.26 ± 0.01	1.03 ± 0.14	2.65 ± 1.13	0.00	0.00	0.00	46.06 ± 0.16	…
SDSS J022205.54+004335.2	0.12 ± 0.01	0.17 ± 0.01	1.04 ± 0.13	2.11 ± 1.03	0.00	0.00	0.00	46.14 ± 0.05	…
HE 0251−5550	1.70 ± 0.04	1.91 ± 0.04	7.57 ± 0.18	18.63 ± 1.00	30.76 ± 6.37	27.70 ± 6.90	15.62 ± 7.57	46.98 ± 0.13	$12.41^{+0.23}_{-0.18}$
SDSS J031712.23−075850.3	0.12 ± 0.01	0.13 ± 0.01	0.46 ± 0.17	2.05 ± 1.29	0.00	0.00	0.00	46.03 ± 0.36	…
SDSS J075547.83+220450.1	0.58 ± 0.02	0.85 ± 0.03	2.98 ± 0.18	5.70 ± 1.04	0.00	0.00	0.00	46.52 ± 0.02	…
SDSS J081127.44+461812.9	0.51 ± 0.01	0.89 ± 0.02	3.26 ± 0.15	7.13 ± 1.08	44.00 ± 6.40	25.99 ± 6.87	0.00	46.55 ± 0.09	$12.92^{+0.06}_{-0.09}$
SDSS J081940.58+082357.9	0.67 ± 0.02	0.72 ± 0.02	2.49 ± 0.20	6.88 ± 1.89	0.00	0.00	0.00	46.85 ± 0.16	…
SDSS J082138.94+121729.9	0.62 ± 0.02	0.52 ± 0.02	0.81 ± 0.18	3.05 ± 1.62	0.00	0.00	0.00	46.39 ± 0.28	…
SDSS J083249.39+155408.6	0.34 ± 0.01	0.55 ± 0.03	4.17 ± 0.24	7.22 ± 1.83	0.00	0.00	0.00	46.67 ± 0.02	…
SDSS J084846.10+611234.6	1.28 ± 0.03	1.49 ± 0.03	3.79 ± 0.15	8.78 ± 0.95	0.00	0.00	0.00	46.63 ± 0.11	…
SDSS J085417.61+532735.2	1.01 ± 0.02	1.23 ± 0.03	3.70 ± 0.17	7.27 ± 1.04	0.00	0.00	0.00	46.65 ± 0.04	…
SDSS J085825.71+005006.7	0.13 ± 0.01	0.18 ± 0.01	0.82 ± 0.16	2.35 ± 1.45	0.00	0.00	0.00	46.25 ± 0.18	…
SDSS J085856.00+015219.4	0.46 ± 0.01	0.80 ± 0.02	3.48 ± 0.16	8.63 ± 1.03	0.00	0.00	0.00	46.56 ± 0.14	…
SDSS J085959.14+020519.7	0.15 ± 0.01	0.22 ± 0.01	1.02 ± 0.13	3.27 ± 1.06	0.00	0.00	0.00	46.41 ± 0.22	…
SDSS J090444.33+233354.0	1.07 ± 0.03	1.39 ± 0.03	4.57 ± 0.17	8.57 ± 1.24	0.00	0.00	0.00	46.66 ± 0.03	…
SDSS J091054.79+023704.5	0.15 ± 0.01	0.14 ± 0.01	0.38 ± 0.16	2.88 ± 1.15	0.00	0.00	0.00	46.27 ± 0.56[b]	…
SDSS J091247.59−004717.3	0.14 ± 0.01	0.22 ± 0.01	1.21 ± 0.17	2.76 ± 1.25	0.00	0.00	0.00	46.37 ± 0.09	…
SDSS J092024.44+662656.7	0.45 ± 0.01	0.87 ± 0.03	3.33 ± 0.13	6.14 ± 0.93	80.71 ± 4.47	70.74 ± 4.99	29.39 ± 5.62	46.38 ± 0.07	$13.14^{+0.01}_{-0.02}$
SDSS J092325.25+453222.2	0.47 ± 0.01	0.39 ± 0.02	1.44 ± 0.16	4.35 ± 1.50	0.00	0.00	0.00	46.70 ± 0.19	…
SDSS J092849.24+504930.5	0.32 ± 0.01	0.50 ± 0.02	2.37 ± 0.12	5.79 ± 0.82	75.14 ± 4.23	60.68 ± 4.49	44.55 ± 5.26	46.47 ± 0.13	$13.21^{+0.01}_{-0.02}$
SDSS J095112.84+025527.3	0.19 ± 0.01	0.28 ± 0.01	1.03 ± 0.16	4.15[c]	0.00	0.00	0.00	46.05 ± 0.18	…

Table 2
(Continued)

ID	$F_{3.4\mu m}$ (mJy)	$F_{4.6\mu m}$ (mJy)	$F_{12\mu m}$ (mJy)	$F_{22\mu m}$ (mJy)	$F_{250\mu m}$[a] (mJy)	$F_{350\mu m}$[a] (mJy)	$F_{500\mu m}$[a] (mJy)	log $L_{5\mu m}$ (erg s^{-1})	log L_{SF} $L_{\odot}$
SDSS J095434.93+091519.6	0.14 ± 0.01	0.16 ± 0.01	1.07 ± 0.18	2.53 ± 1.26	78.44 ± 4.09	101.53 ± 3.56	88.02 ± 4.04	46.50 ± 0.10	$13.66^{+0.01}_{-0.01}$
SDSS J100515.99+480533.3	0.38 ± 0.01	0.46 ± 0.02	1.62 ± 0.12	3.56 ± 0.99	0.00	0.00	0.00	46.30 ± 0.09	…
SDSS J101120.39+031244.5	0.58 ± 0.02	0.74 ± 0.02	2.60 ± 0.17	5.28 ± 1.20	0.00	0.00	0.00	46.52 ± 0.05	…
SDSS J102325.31+514251.0	0.43 ± 0.01	0.39 ± 0.01	1.42 ± 0.12	3.51 ± 1.10	20.96 ± 6.39	18.39 ± 6.89	22.52 ± 7.44	46.65 ± 0.11	$12.84^{+0.13}_{-0.16}$
SDSS J102719.13+584114.3	0.24 ± 0.01	0.51 ± 0.02	2.10 ± 0.12	3.15 ± 1.09	0.00	0.00	0.00	46.14 ± 0.07	…
SDSS J104018.51+572448.1	0.41 ± 0.01	0.38 ± 0.01	1.03 ± 0.11	1.87 ± 0.85	0.00	0.00	0.00	46.47 ± 0.03	…
SDSS J104121.88+563001.2	0.25 ± 0.01	0.45 ± 0.01	2.21 ± 0.14	7.63 ± 0.97	0.00	0.00	0.00	46.27 ± 0.36[b]	…
SDSS J104442.15+381257.2	0.20 ± 0.01	0.27 ± 0.01	0.79 ± 0.15	3.97[c]	0.00	0.00	0.00	45.79 ± 0.18	…
SDSS J104639.43+584047.7	0.13 ± 0.01	0.16 ± 0.01	1.08 ± 0.12	2.92 ± 0.91	0.00	0.00	0.00	46.40 ± 0.07	…
SDSS J104809.19+570241.9	0.18 ± 0.01	0.24 ± 0.01	1.60 ± 0.12	5.01 ± 0.91	0.00	0.00	0.00	46.63 ± 0.07[b]	…
SDSS J105146.05+592214.0	0.17 ± 0.01	0.21 ± 0.01	0.69 ± 0.14	2.62 ± 1.25	0.00	0.00	0.00	46.25 ± 0.29	…
SDSS J105902.04+580848.6	0.45 ± 0.01	0.64 ± 0.02	2.39 ± 0.14	5.69 ± 1.13	24.39 ± 2.06	19.06 ± 1.98	0.00	46.42 ± 0.13	$12.69^{+0.03}_{-0.03}$
SDSS J110445.39+573643.9	0.13 ± 0.01	0.17 ± 0.01	0.80 ± 0.14	2.28 ± 1.21	0.00	0.00	0.00	46.15 ± 0.19	…
SDSS J111313.29+102212.4	0.77 ± 0.02	1.14 ± 0.03	4.61 ± 0.19	11.26 ± 1.20	0.00	0.00	0.00	46.72 ± 0.13	…
SDSS J111928.37+130251.0	0.25 ± 0.01	0.26 ± 0.02	1.23 ± 0.17	2.21 ± 1.27	0.00	0.00	0.00	46.13 ± 0.02	…
SDSS J113157.72+191527.7	0.47 ± 0.01	0.53 ± 0.02	1.32 ± 0.17	3.55 ± 1.27	0.00	0.00	0.00	46.46 ± 0.15	…
SDSS J113627.81+541504.4	0.20 ± 0.01	0.25 ± 0.01	0.99 ± 0.12	1.72 ± 1.09	0.00	0.00	0.00	46.35 ± 0.03	…
SDSS J114412.76+315800.8	0.15 ± 0.01	0.18 ± 0.01	1.04 ± 0.13	2.28 ± 0.88	30.52 ± 6.34	32.53 ± 6.75	26.82 ± 7.44	46.42 ± 0.07	$13.08^{+0.06}_{-0.13}$
SDSS J115517.34+634622.0	0.90 ± 0.02	0.77 ± 0.02	1.54 ± 0.12	4.05 ± 1.01	33.40 ± 7.82	16.84 ± 8.18	13.66 ± 9.55	46.52 ± 0.15	$12.90^{+0.10}_{-0.14}$
SDSS J122307.52+103448.1	0.16 ± 0.01	0.19 ± 0.01	0.78 ± 0.14	2.52[c]	0.00	0.00	0.00	46.08 ± 0.18	…
SDSS J122654.39−005430.6	0.39 ± 0.01	0.47 ± 0.02	1.11 ± 0.16	3.99 ± 1.71	0.00	0.00	0.00	46.33 ± 0.27	…
SDSS J123132.37+013814.0	0.11 ± 0.01	0.10 ± 0.01	0.40 ± 0.13	3.49 ± 1.16	0.00	0.00	0.00	46.31 ± 0.61[b]	…
SDSS J123515.83+630113.3	0.45 ± 0.01	0.73 ± 0.02	3.09 ± 0.14	6.01 ± 0.80	30.82 ± 6.34	37.29 ± 6.87	26.22 ± 7.49	46.56 ± 0.04	$12.73^{+0.06}_{-0.07}$
SDSS J123637.45+615814.3	0.17 ± 0.01	0.24 ± 0.01	0.80 ± 0.11	1.87 ± 0.99	0.00	0.00	0.00	46.06 ± 0.11	…
SDSS J123714.60+064759.5	0.43 ± 0.01	0.63 ± 0.02	3.80 ± 0.15	11.81 ± 0.99	94.20 ± 3.68	94.26 ± 3.88	54.41 ± 4.56	46.91 ± 0.21[b]	$13.43^{+0.01}_{-0.00}$
SDSS J123743.08+630144.8	0.12 ± 0.01	0.12 ± 0.01	0.80 ± 0.08	2.72 ± 0.70	25.83 ± 2.52	20.00 ± 2.47	13.63 ± 3.00	46.46 ± 0.24	$12.98^{+0.03}_{-0.04}$
SDSS J124302.42+521009.8	0.16 ± 0.01	0.23 ± 0.01	1.14 ± 0.13	2.53 ± 1.31	0.00	0.00	0.00	46.22 ± 0.09	…
SDSS J124456.98+620143.0	0.16 ± 0.01	0.17 ± 0.01	0.90 ± 0.09	2.00 ± 0.80	0.00	0.00	0.00	46.30 ± 0.08	…
SDSS J124748.44+042627.1	0.16 ± 0.01	0.18 ± 0.01	0.37 ± 0.18	2.65 ± 1.33	0.00	0.00	0.00	46.07 ± 0.55	…
SDSS J125125.36+412000.4	0.12 ± 0.01	0.16 ± 0.01	1.34 ± 0.12	3.30[c]	48.71 ± 3.58	39.74 ± 3.90	27.13 ± 4.85	46.48 ± 0.17[b]	$13.25^{+0.02}_{-0.02}$
SDSS J125819.24+165717.6	0.34 ± 0.01	0.47 ± 0.02	2.24 ± 0.14	3.71 ± 1.05	49.46 ± 5.30	40.48 ± 6.00	32.27 ± 6.70	46.51 ± 0.03	$13.12^{+0.03}_{-0.04}$
SDSS J131215.22+423900.8	0.23 ± 0.01	0.29 ± 0.01	1.22 ± 0.13	3.18 ± 1.00	0.00	0.00	0.00	46.29 ± 0.15	…
SDSS J132809.59+545452.7	0.26 ± 0.01	0.44 ± 0.01	2.12 ± 0.11	5.73 ± 0.78	77.97 ± 6.34	73.04 ± 6.79	46.97 ± 7.48	46.33 ± 0.18[b]	$13.09^{+0.08}_{-0.03}$
SDSS J133219.65+622715.9	0.09 ± 0.00	0.09 ± 0.01	0.33 ± 0.08	1.46 ± 0.71	29.83 ± 2.46	26.35 ± 2.45	17.72 ± 2.86	46.06 ± 0.34[b]	$13.07^{+0.02}_{-0.02}$
SDSS J133907.13+131039.6	0.42 ± 0.01	0.48 ± 0.02	1.05 ± 0.13	3.47[c]	0.00	0.00	0.00	46.00 ± 0.18	…
SDSS J135559.03−002413.6	0.26 ± 0.01	0.41 ± 0.02	1.63 ± 0.10	2.89 ± 0.82	19.03 ± 2.66	24.26 ± 2.66	0.00	46.23 ± 0.02	$12.67^{+0.03}_{-0.04}$
SDSS J141819.22+044135.0	0.19 ± 0.01	0.34 ± 0.01	1.50 ± 0.09	3.16 ± 0.63	49.11 ± 6.34	57.63 ± 6.88	52.43 ± 7.52	46.31 ± 0.07	$13.04^{+0.04}_{-0.04}$
SDSS J142539.01+331009.5	0.26 ± 0.01	0.28 ± 0.01	0.55 ± 0.11	2.49[c]	0.00	0.00	0.00	45.75 ± 0.18	…
SDSS J142539.98+344843.5	0.50 ± 0.01	0.80 ± 0.02	3.58 ± 0.15	8.69 ± 1.20	34.52 ± 2.45	19.27 ± 2.75	8.75 ± 3.13	46.60 ± 0.13[b]	$12.79^{+0.03}_{-0.03}$
SDSS J142912.87+340959.0	0.24 ± 0.01	0.37 ± 0.01	1.51 ± 0.09	5.19 ± 0.73	34.42 ± 1.29	25.05 ± 1.23	15.48 ± 1.51	46.29 ± 0.27[b]	$12.88^{+0.01}_{-0.01}$
SDSS J143543.71+342906.4	0.30 ± 0.01	0.31 ± 0.01	1.13 ± 0.10	1.92 ± 0.76	0.00	0.00	0.00	46.16 ± 0.02	…
SDSS J143941.92+332519.5	0.20 ± 0.01	0.36 ± 0.01	1.83 ± 0.09	3.44 ± 0.75	0.00	0.00	0.00	46.25 ± 0.03	…
SDSS J143954.64+334658.9	0.09 ± 0.00	0.05 ± 0.01	0.22 ± 0.12	1.57 ± 0.76	0.00	0.00	0.00	46.07 ± 0.53	…
SDSS J145706.34+220548.6	0.07 ± 0.00	0.08 ± 0.01	0.25 ± 0.11	1.55[c]	0.00	0.00	0.00	45.72 ± 0.18	…
SDSS J155744.01+330231.0	0.12 ± 0.00	0.15 ± 0.01	0.68 ± 0.07	1.61 ± 0.58	0.00	0.00	0.00	46.23 ± 0.10	…

Table 2
(Continued)

ID	$F_{3.4\mu m}$ (mJy)	$F_{4.6\mu m}$ (mJy)	$F_{12\mu m}$ (mJy)	$F_{22\mu m}$ (mJy)	$F_{250\mu m}$[a] (mJy)	$F_{350\mu m}$[a] (mJy)	$F_{500\mu m}$[a] (mJy)	$\log L_{5\mu m}$ (erg s^{-1})	$\log L_{SF}$ $L_{\odot}$
SDSS J161238.26+532255.0	0.32 ± 0.01	0.47 ± 0.01	1.78 ± 0.07	3.99 ± 0.48	46.19 ± 6.06	51.48 ± 4.04	36.51 ± 4.90	46.22 ± 0.02	$12.83^{+0.03}_{-0.03}$
SDSS J210831.56−063022.5	0.49 ± 0.01	0.82 ± 0.02	4.10 ± 0.19	7.72 ± 1.06	41.10 ± 6.36	27.65 ± 6.90	20.45 ± 7.54	46.65 ± 0.03	$12.82^{+0.14}_{-0.16}$
SDSS J212329.46−005052.9	1.44 ± 0.03	2.29 ± 0.05	8.96 ± 0.25	21.02 ± 1.15	34.58 ± 6.38	30.98 ± 6.86	18.13 ± 7.54	47.00 ± 0.12	$12.45^{+0.19}_{-0.15}$
LBQS 2154−2005	0.51 ± 0.01	0.92 ± 0.03	4.34 ± 0.20	8.93 ± 1.33	34.67 ± 6.38	17.30 ± 6.85	0.00	46.50 ± 0.06	$12.73^{+0.09}_{-0.24}$
HE 2156−4020	0.59 ± 0.02	1.03 ± 0.03	4.38 ± 0.16	9.37 ± 0.96	0.00	0.00	0.00	46.79 ± 0.07	…
2QZ J221814.4−300306	0.35 ± 0.01	0.46 ± 0.02	1.90 ± 0.16	3.95 ± 1.13	0.00	0.00	0.00	46.36 ± 0.07	…
2QZ J222006.7−280324	1.97 ± 0.04	2.12 ± 0.05	7.84 ± 0.24	19.31 ± 1.41	39.65 ± 6.39	27.99 ± 6.87	19.43 ± 7.51	47.02 ± 0.13	$12.49^{+0.26}_{-0.15}$
SDSS J222256.11−094636.2	0.42 ± 0.01	0.44 ± 0.02	1.85 ± 0.15	4.53 ± 1.33	0.00	0.00	0.00	46.59 ± 0.12	…
SDSS J233446.40−090812.2	0.29 ± 0.01	0.31 ± 0.01	1.43 ± 0.16	2.21 ± 1.05	50.77 ± 6.90	56.18 ± 7.36	37.35 ± 8.30	46.51 ± 0.07	$13.35^{+0.04}_{-0.06}$

Notes.
[a] This value is zero if the source was not detected at a significance larger than 3σ at 250 μm.
[b] Weak near-infrared source.
[c] 2σ upper confidence limit in the corresponding *WISE* band.

Table 3
Fluxes and luminosities for Median and Mean Stacks

	$\log L_{1350}$ (erg s^{-1})	# of Sources in the Stack	$z_{\rm nominal,stack}$	$F_{250\ \mu{\rm m,stack}}$ (mJy)	$F_{350\ \mu{\rm m,stack}}$ (mJy)	$F_{500\ \mu{\rm m,stack}}$ (mJy)	$\log \lambda L_{250}$ (erg s^{-1})	$\log \lambda L_{350}$ (erg s^{-1})	$\log \lambda L_{500}$ (erg s^{-1})
Median stack	46.7–48	28	2.5	8.16[6.50, 9.95]	6.15[4.07, 7.68]	3.89[1.98, 5.95]	45.13[44.51, 45.38]	45.18[44.87, 45.36]	44.45[44.94, 45.17]
	46.5–46.7	38	2.5	8.0[6.27, 9.65]	4.8[3.52, 6.33]	4.59[3.26, 6.19]	45.47[45.29, 45.60]	45.17 [44.94, 45.32]	45.09[44.54, 45.32]
Mean stack	46.7–48	28	2.5	8.16[6.50, 9.95]	6.15[4.07, 7.68]	3.89[1.98, 5.95]	45.62[45.44, 45.74]	45.24[45.04, 45.38]	45.17[44.94, 45.31]
	46.5–46.7	38	2.5	10.32[7.88, 12.71]	6.27[4.76, 7.54]	5.16[3.64, 6.56]	45.64[45.46, 45.77]	45.32[45.18, 45.43]	45.14[44.98, 45.26]

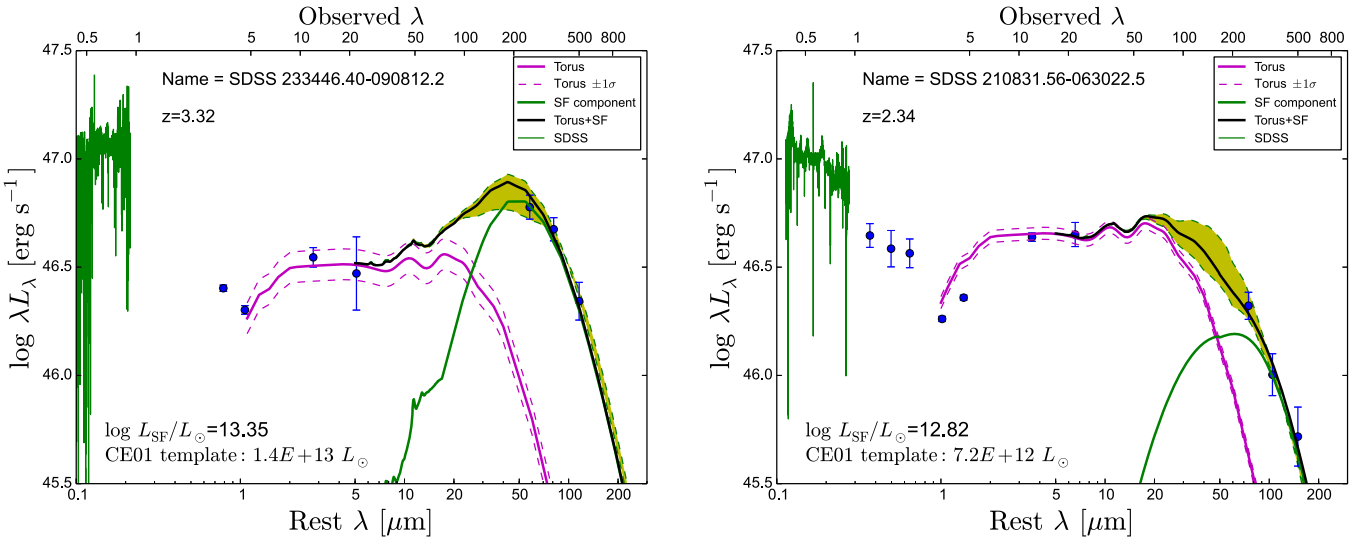

Figure 2. Examples of combined SED fittings for objects with different $L_{5\mu m}/L_{SF}$. SDSS data are shown in green, and NIR (J,H,K) and MIR (*WISE*) data as blue points. The shaded area shows the range of SF templates used in the fit. The key to the various curves used in the fit is given in the top right of each panel.

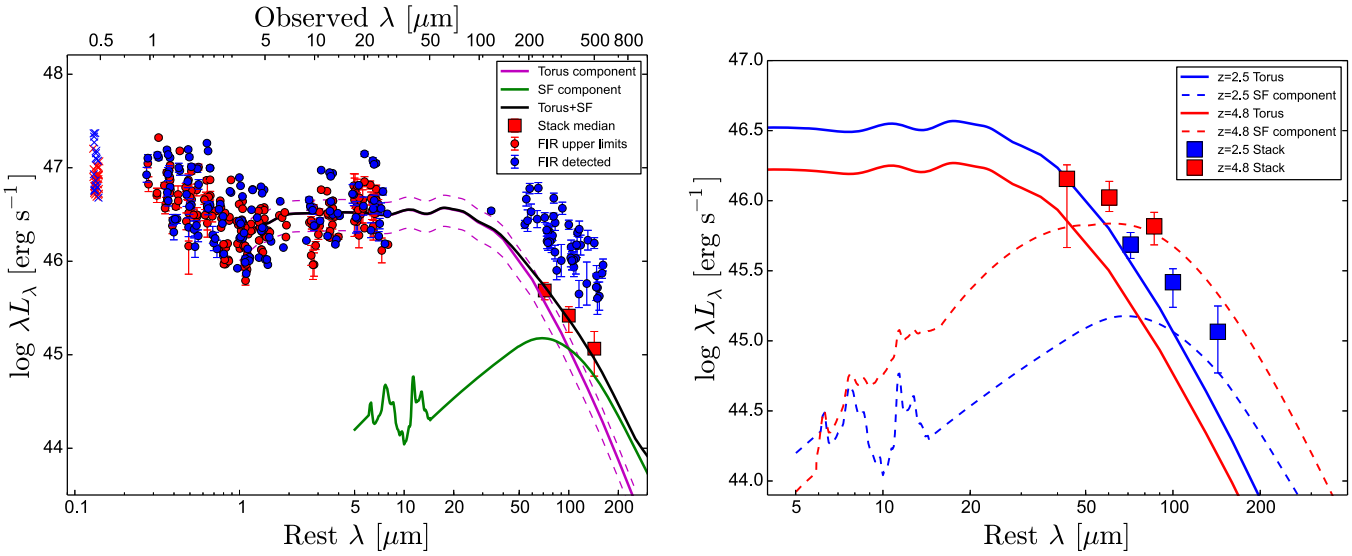

Figure 3. Left: summary of the observed properties of the sources in the high luminosity group (log $L_{1350} > 46.7$). "X" symbols denote the observed L_{1350}. The magenta line is the median Mor & Netzer (2012) torus and the green line the SF template fitted to the median stack. *Herschel*-detected sources are shown in blue and undetected sources in red (circles for upper limits and squares for the median stack). All symbols are also shown in the upper insert. Note the great similarity between the detected and undetected sources over the entire wavelength range, except for the FIR. Right: a comparison of the torus and FIR stacks in the present sample (blue) and the $z \simeq 4.8$ Netzer et al. (2014) sample (red). Note that the SFR in the higher redshift sample is larger, while the mean torus luminosity is smaller.

smaller than those in the SPIRE bands, which will severely bias the combined analysis. We search for the combination of the Chary & Elbaz (2001) template and scaling that produces the lowest/highest L_{SF} within $\chi^2 < \chi^2_{min} + 1$ and take these values as our low/high L_{SF} 1-σ limits listed in Table 2. Figure 2 shows two examples of combined fits for *Herschel*-detected sources with different SF templates.

We followed a similar procedure to fit the stacked spectra. Because we have *WISE* data for all the sources, we can create two median torus templates for the two subgroups as defined by the threshold luminosity L_{1350}. The scatter in the torus luminosity in the two groups is small and this procedure results in well-defined torus templates. The two are processed separately because their median $L_{5\mu m}$ differ by approximately 0.3 dex, which has an effect on the combined torus-SF fit. We measured the stack L_{SF} in a manner that is similar to the one used to fit the detected sources. The stack SPIRE fluxes are only 2–4 times larger than the predicted torus fluxes, and the uncertainties on the resulting SFRs are large. As in the case of the detected sources, we tried a "free-shape" approach (all the SEDs in the relevant range of the template libraries) and the more conventional way of using the actual luminosities in the SF library. Figure 3 shows the fitted SED of the median stacked spectrum of the more luminous $z = 2$–3.5 subsample, together with the *WISE* data. The formally measured SFR is 74 $M_{\odot}$ yr^{-1} with an acceptable range 47–100$M_{\odot}$ yr^{-1}. The application of the second approach (i.e., luminosities obtained directly from the template library) results in SFR within 20% of this number. Finally, we repeated the same procedure to obtain mean stacks for the two luminosity groups.

Figure 3 also shows the same method applied to the Netzer et al. (2014) $z \simeq 4.8$ sample. The fits quality is similar but there

Table 4
Mean and Median SFRs for Detected and Undetected *Herschel* Sources and the Entire Sample

	SPIRE Detected		SPIRE Stacks		All Sources
	Mean	Median	Mean	Median	Mean
$\log L_{1350} < 46.7$	$N = 19$		$N = 38$		$N = 57$
SFR ($M_\odot$ yr$^-$)	1415^{+707}_{-472}	1160^{+596}_{-485}	151^{+29}_{-33}	115^{+26}_{-28}	572
$\log L_{1350} > 46.7$	$N = 15$		$N = 28$		$N = 43$
SFR ($M_\odot$ yr$^-$)	868^{+553}_{-338}	683^{+560}_{-420}	145^{+29}_{-33}	74^{+26}_{-27}	397
All sources	$N = 34$		$N = 66$		$N = 100$
SFR ($M_\odot$ yr$^-$)	1176^{+477}_{-339}	1010^{+706}_{-503}			497

Note. N is the number of sources in each group and the uncertainties reflect the 16 and 84 percentiles.

is a significant difference in the ratio L_{SF}/L_{torus}. While the higher redshift sample is of lower AGN luminosity, and hence lower L_{torus}, its mean SFR is higher by a factor of approximately 3. The lower redshift of the present sample allows us to go significantly below the SFR of the most massive SF galaxies at $z = 2$–3.5 (e.g., Schreiber et al. 2015), while for the $z \simeq 4.8$ sample, the mean SFR of the undetected sources is very similar to that expected for the most massive SF hosts at this redshift. We come back to these points in Section 3.

3. RESULTS AND DISCUSSION

The new observations presented here show several characteristics of the most luminous AGNs in the universe, in particular the relationships between SFR in the host, the intrinsic AGN luminosity, and dust emission by the torus. In this section we provide a detailed discussion of the new results and compare them with those obtained for other samples of high luminosity AGNs.

The left panel of Figure 3 provides a visual summary of many of the properties of the *Herschel*-detected and undetected sources in the subsample with $\log L_{1350}$ (erg s^{-1}) > 46.7. The diagram demonstrates the similarity of *Herschel*-detected and undetected sources across the UV–optical–NIR–MIR range, and the large range in L_{SF} for these sources. The median and mean SFRs for the various groups, and the entire sample, are summarized[6] in Table 4.

3.1. Torus and SF Emission at $z > 5$

A recent detailed discussion of SF and AGN emission at very high redshift is given in Leipski et al. (2014). This work presents data for 69 $z > 5$ high luminosity AGNs observed by *Spitzer*, *Herschel*, and various sub-millimeter telescopes. The sample was not selected in a systematic way and it is not clear how well it represents the $z > 5$ AGN population. The total number of FIR-detected sources is 7–11, depending on the number of *Herschel* bands required to define a source as "FIR-detected" (Leipski et al. require detection in four *Herschel* bands, from both PACS and SPIRE). Leipski et al. (2014) used a three-component dust emission model to measure what they defined as hot-dust NIR blackbody emission, warm dust torus emission, and cold dust SF emission. Because their way of modeling the IR SED is rather different from ours, we used the data in their paper and our assumed torus SED, to remeasure the FIR and dust emission in all their *Herschel*/SPIRE-detected sources. Two objects in their samples have only 250 μm detections, two others both 250 and 350 μm detections, and seven with detections in all three bands. We followed our fitting procedure, this time with PACS and *Spitzer* data given in Leipski et al. (2014), and the same torus model, to derive L_{SF} and L_{torus} for these 11 sources. We could not find a satisfactory solution for the 250 μm-only sources, and for one of the sources with both 250 and 350 μm detections. For the other eight sources we found reliable L_{SF} estimates that, for the seven sources in common, are similar to the L_{SF} found by Leipski et al. (2014). Five of the eight sources belong in the category of weak-NIR AGN, which is a much larger fraction than in the general population. Given the very small number of *Herschel*-detected sources, we consider this to be only tentative evidence for a larger fraction of weak-NIR sources at high redshift.

Regarding the estimate of L_{AGN}, we used L_{5100} as listed in Leipski et al. (2014) with a bolometric correction factor of 4, which is consistent with our bolometric correction factor for L_{1350} (Trakhtenbrot & Netzer 2012). This method gives values that are 30%–40% higher than the those estimated by them from direct integration over the rest-frame wavelength 0.1–1 μm. The two estimates are consistent because the Leipski et al. (2014) estimates do not take into account the luminosity of the $\lambda < 0.1$ μm part of the SED, which is included in our estimates of L_{AGN}.

3.2. L_{AGN} and L_{SF} at $z = 2$–3.5

We have looked for possible correlations between L_{AGN} and L_{SF} in every AGN discussed in this paper, and compared them with various correlations suggested in the literature. In doing so we take into consideration the fact that the methods used for selecting the samples (e.g., X-ray selection versus FIR selection) greatly influence the results. This was explained in detail in Section 1, where we also gave many relevant references. Because our sample is optically selected, the ones more relevant to the present study are those based on the AGN properties (e.g., X-ray flux).

First we focus on correlations suggested for "AGN-dominated" systems (i.e., those with $L_{AGN} > L_{SF}$). Such correlations were discussed in Netzer (2009) and Netzer et al. (2014), and can be expressed as $\log L_{SF} = 0.7 \log L_{AGN} + 12.9$. This relationship is an attempt to fit, by eye, a combination of a large number of low luminosity AGNs and a small number of highly luminous AGNs. It is not based on a formal regression analysis because the number

[6] Note that we do not provide proper uncertainties on the mean and median SFRs of the entire sample because we did not stack all the undetected sources together. The numbers in the last column are simple means of the other columns.

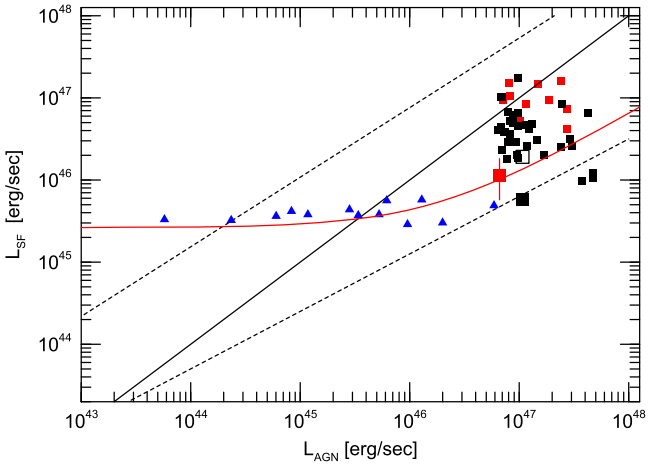

Figure 4. L_{SF} vs. L_{AGN} for various representative samples at low and intermediate redshifts, and our two high-redshift samples at $z = 2$–3.5 and $z \simeq 4.8$. Blue triangles: Stanley et al. (2015). Full black squares: the present sample (the big square is the mean of all the undetected sources). Open black square: the mean of the entire sample. Red squares: Netzer et al. (2014; the big square represents the stacked source). Red solid line: the Rosario et al. (2012) fit to the $1.5 < z < 2.5$ AGNs scaled up by a factor 2. Upper dashed black line: the Delvecchio et al. (2015) fit to their SF-dominated sources. Lower dashed line: Netzer (2009) fit to AGN-dominated sources. Solid black line: $L_{SF} = L_{AGN}$.

of low luminosity sources far exceeds the number of very luminous systems, thus biasing any attempt to obtain a meaningful correlation that spans 4–5 orders of magnitude in luminosity. It is also obtained for individual sources and does not involve mean or median properties. The second comparison is with the Stanley et al. (2015) sample of X-ray detected AGNs at redshifts 0.2–2.5. In this case, most of the objects are not detected by *Herschel*, and the authors used a survival analysis to obtain mean FIR fluxes. This approach is similar to the one used by Rosario et al. (2012), who used stacking of *Herschel* data, and the results of the two studies are in good agreement except, perhaps, at the highest L_{AGN} end. The data we compared with our observations are those found in the redshift range $1.87 < z < 2.08$, which correspond to the most luminous objects in these samples. Finally, we also examine the correlation for "SF-dominated" sources suggested by Delvecchio et al. (2015) for their $0.15 < z < 2.3$ sources. This correlation can be expressed as $\log L_{AGN} = -9.32 + 1.18 L_{SF}$. It is based on a systematic study of FIR, *Herschel*-selected sources in the COSMOS and GOODS fields where SF luminosities were obtained from measured FIR SEDs and L_{AGN} from stacked X-ray (*Chandra*) data (~10% detections and ~90% undetected sources). The results of this work are in good agreement with the earlier results of Chen et al. (2013) for SFR $> 1\ M_{\odot}\,\mathrm{yr}^{-1}$.

In order to use consistent estimates of L_{AGN}, we recalibrated the values obtained by Netzer et al. (2014) for their $z \simeq 4.8$ sample by adopting the approximation used here of $L_{AGN} = 2\ L_{1350}$. The new values are within 20% of the numbers found by Netzer et al. (2014). The X-ray based estimates of L_{AGN} for other samples considered here were obtained from the original papers using the bolometric correction factors from Marconi et al. (2004). We prefer this direct approach rather than the one used by Stanley et al. (2015), who first compared the X-ray and MIR luminosities and then used correlations between MIR luminosity and L_{AGN}.

Figure 4 shows L_{SF} versus L_{AGN} for various representative samples and our own samples for $z = 2$–3.5 and $z \simeq 4.8$. The additional samples are from Delvecchio et al. (2015), where we only show the best-fit line, the Stanley et al. (2015) sample, the curve fitted by Rosario et al. (2012) to their $1.5 < z < 2.5$ group of sources scaled up by a factor 2 (Rosario et al. 2012 used the measured 60 μm luminosity rather than L_{SF}), and the fit to the Netzer (2009) relationship. For the present sample, we show all individually detected sources, the mean for the stacked sources, and the mean for the entire sample.

The comparison is illuminating. It shows that most of the $z > 2$ AGN hosts (those in the stacks) have roughly the same L_{SF} as the mean measured in the lower redshift samples that include detected sources. However, the L_{SF} of the *Herschel*-detected sources exceeds this value by about an order of magnitude. As a result, the mean L_{SF} in our sample (shown as an open black square) is significantly higher than the typical values obtained by Stanley et al. (2015) over a similar redshift range. The main reason for this is probably related to the fact that very high L_{AGN} objects are missing from studies based on small fields, like COSMOS, that do not properly sample the high end of the AGN luminosity function.

3.3. L_{AGN} and L_{SF} Across Time

The high-redshift samples studied here can be compared with earlier works addressing stellar-mass growth via SF at similar epochs. In particular, we want to compare the newly measured SFRs with studies of the main sequence (MS) of star-forming galaxies and the IR luminosity function (IRLF) of high-redshift galaxies. Out of the numerous papers published on the correlation of stellar mass, SFR, and sSFR, (e.g., Daddi et al. 2007; Rodighiero et al. 2011; Wuyts et al. 2011; Speagle et al. 2014 and references therein) we chose to compare our results with those of Schreiber et al. (2015) that cover a very large range of stellar masses for all redshifts between 0 and 5. This study is based on FIR measurements and thus avoids the uncertainties associated with UV dust attenuation. It is also quite complete in terms of high-mass galaxies and is in good agreement with the systematic work of Speagle et al. (2014), which includes a detailed comparison and calibration of different methods. For the definition of the MS, we use the parameterization given in Equation (9) of Schreiber et al. (2015) that suggests a continuous growth of sSFR with redshift for the most massive galaxies, up to $z \sim 4$. The conversion factor from SFR to L_{SF} used by these authors is a factor of 1.7 larger than the one used here, due to the different assumed IMF, and the following calculations take this into account. Finally, we assume that the width of the MS close to its high-mass end is ± 0.3 dex, a value that is consistent with most of the references listed above, but at such high redshifts is quite uncertain.

There are fewer papers about LFs at high redshift (see Madau & Dickinson 2014 and references therein). The specific work used here is Gruppioni et al. (2013), which focuses on the IRLF and is based on *Herschel* observations. The highest redshifts considered in this paper are $z \sim 4$. Stellar mass functions for these fields are shown by Schreiber et al. (2015; their Figure 3) and are basically identical to the ones presented by Ilbert et al. (2013) and Madau & Dickinson (2014).

The $z = 2$–3.5 and $z \simeq 4.8$ samples represent well the population of the most luminous AGNs in these redshift intervals. The $z > 5$ sample was chosen in a different way, and is less complete in this respect. However, it includes many of the most luminous objects in this redshift range and hence provides some indication about the overall distribution in L_{AGN}

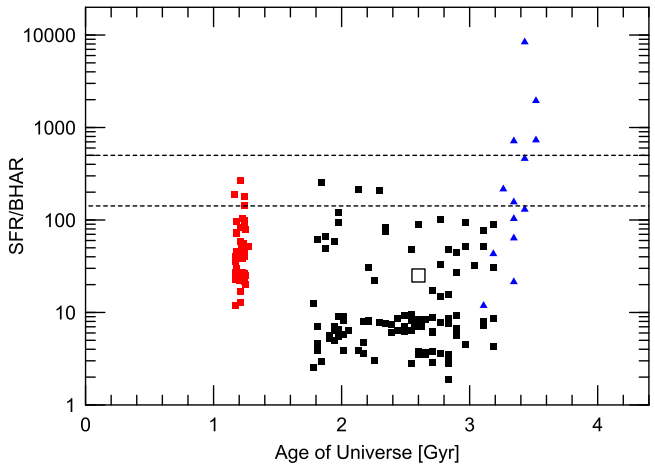

Figure 5. SFR/BHAR as a function of cosmic time for the sources and samples shown in Figure 4, using the same symbols and colors. In this diagram we show *all* individual sources from the stacks assuming the corresponding mean SFRs. The dashed horizontal lines mark the two ratios explained in the text, SFR/BHAR = 500 ("typical" of local AGNs) and SFR/BHAR = 142 ($L_{SF} \simeq L_{AGN}$).

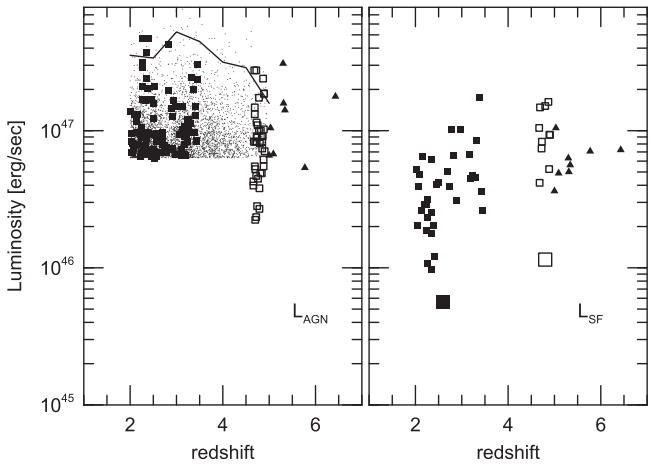

Figure 6. L_{AGN} (left panel) and L_{SF} (right panel) as functions of redshift for *Herschel*-observed sources in the Leipski et al. (2014; filled triangles, detections only), Netzer et al. (2014; small open squares for detections and a large open square for the stack), the present samples (small filled squares for detections and large filled squares for the stacks), and the parent SDSS sample (small points). The solid line in the left panel connects the 10th most luminous AGNs in the Shen et al. (2011) sample in redshift bins separated by 0.5.

and L_{SF}. The overall range in L_{AGN} of the three high-redshift samples is about a factor of 10. The range in L_{SF} is more difficult to define because approximately 70% of the sources are not detected by *Herschel*. Using our individual detections, and the mean and median stacks, we find this range to be approximately 1.6 dex. Obviously the stacks may include completely quenched hosts.

We first consider the ratio of the SFR to BH accretion rate (BHAR) as a function of cosmic time for the SPIRE-detected sources in the redshift ranges 2–3.5, ≈4.8 and >5. To do this we assume a mass-to-radiation conversion efficiency of $\eta = 0.1$ corresponding to thin accretion disks with a spin parameter of ∼0.7, which is consistent with the high spin values for very massive BHs measured by Capellupo et al. (2015). The results are shown in Figure 5, where the individual points have the same meanings as in Figure 4. In the diagram we mark the line corresponding to SFR/BHAR = 500, which is the ratio of stellar mass to BH mass in the local universe for galaxies hosting BHs with $M_{BH} \sim 10^8\,M_{\odot}$ with a bulge mass that is half the total mass of the galaxy (Kormendy & Ho 2013 and references therein). All sources in all three high-redshift samples, except for some of the stacked averages in the Stanley et al. (2015) sample, are well below this line. The detected sources cluster around SFR/BHAR ≃ 80, not far from SFR/BHAR = 142, which corresponds to $L_{SF} \simeq L_{AGN}$ (also marked in the diagram). This accretion rate ratio is very similar to the stellar-to-BH mass ratio for the most massive spheroidal galaxies in the local universe. The undetected sources are all below SFR/BHAR = 10. We also note that the study of type-II radio-loud AGNs by Drouart et al. (2014), which is based on very different ways of estimating BHARs, shows values of SFR/BHAR that are consistent with the ones shown here.

Figure 6 shows the changes with redshift of L_{AGN} and L_{SF} for all the detected sources in the three high-redshift samples, and the stacks in the current sample and in the $z \simeq 4.8$ sample. While the Leipski et al. (2014) sample is less complete, and we do not have information on the undetected sources, it allows us to extend the redshift range to beyond 5. The dependence of the highest L_{AGN} on redshift is not new, but it is similar to what is known from previous studies of large samples like the SDSS, and from the X-ray and optical LFs of AGNs (e.g., Croom et al. 2009; Vestergaard & Osmer 2009; Shen et al. 2011; Trakhtenbrot & Netzer 2012; Ueda et al. 2014; Vito et al. 2014; see however a different view in Vardanyan et al. 2014 regarding the most luminous AGNs based on *WISE* observations). As already shown here, and in Netzer et al. (2014), both the $z \simeq 4.8$ and $z = 2$–3.5 samples represent the population very well and thus reproduce the behavior of the highest luminosity part of the LF. This is also illustrated by the entire parent SDSS sample, shown in the left panel as small points. The left panel of Figure 6 shows a steady increase from very high redshifts up to $z \sim 3$, followed by a decrease at smaller redshifts. This trend is illustrated in a simplistic way by showing a line representing the 10th most luminous source from the Shen et al. (2011) catalog (this way of representation is superior to the median L_{AGN} that reflects only the chosen lower limit on L_{AGN} because of the very steep LF).

The change of L_{SF} with redshift for the hosts of the most luminous AGNs, shown in the right panel, is new and very different. It exhibits a moderate rise from $z = 7$ to $z \sim 4$–5 followed by a decrease at lower redshifts. The diagram shows a hint for an overall decline in L_{SF} from $z = 3.5$ to $z = 2$. Unfortunately, the statistics are rather poor and based on only 34 *Herschel*-detected sources. However, they are in general agreement with studies of IRLFs, such as Gruppioni et al. (2013). Such studies show a steady increase in L_{SF} for the most luminous FIR galaxies from $z = 2$ to $z \sim 4$–5, with a rather uncertain behavior beyond this redshift due to poor statistics. Moreover, the luminosity close to the high luminosity end of the $z \sim 4$–5 IRLF ($\log L_{SF}$ (erg s^{-1}) ∼47) is very similar to the luminosities we measured at the same redshifts. We can thus conclude that the host galaxies of the most luminous AGNs across the redshift range $z = 2$–5 represent well the high luminosity end of the IRLFs at those redshifts. We also note a somewhat similar behavior, based on a smaller number of sources, in the type-II radio-loud sample of Drouart et al. (2014). In summary, the analysis of the most luminous AGNs and their hosts shows that the peak in BH growth rate lags behind the peak SFR of their host galaxies by approximately a

Gyr, corresponding to the difference in cosmic time between redshifts ∼5 and ∼3 under the assumption that we are looking at the same population in these redshifts bins.

Our current sample does not contain a large enough number of AGNs with reliable BH mass measurements, and using such information for only a handful of sources and not others can result in severe biases. We prefer to use estimates of these properties in earlier studies of the highest luminosity AGNs in the same redshift range. The most suitable studies are those of Shemmer et al. (2004) and Netzer et al. (2007), which have a combined number of 44 AGN between $z = 2$ and $z = 3.5$. The luminosity distribution in that sample is different from the one used here, because it contains several AGNs below our lowest $L_{\rm AGN}$ and several others that are even more luminous than the SDSS sources studied here. However, the median $\log(L_{\rm AGN})$ is 46.9, which is merely 0.1 dex below the median value in the present sample. For lack of better information, we assume the same median Eddington ratio for the two samples and adopt the median BH mass in the above combined sample, $10^{9.5}\,M_{\odot}$, as our best estimate for the median BH mass in the current sample.[7] The situation at $z \simeq 4.8$ is better because all objects have reliable BH mass estimates.[8]

Unfortunately, we do not have stellar-mass measurements for any of the sources in the $z = 2$–3.5 and $z \simeq 4.8$ samples. We therefore limit the discussion to a simple scenario where the stellar mass is not very different from the largest MS stellar masses at those redshifts. This is in the range $10^{11-11.5}\,M_{\odot}$ (Schreiber et al. 2015) for the $z \simeq 4.8$ sample, and perhaps somewhat higher at $z = 2$–3.5. Such a scenario is a likely possibility out of several that we are not yet in a position to test. We are going to test the consequences to BH and stellar-mass growth across the redshift range of $z \simeq 4.8$ to $z = 2$–3.5. However, such ideas are rather speculative given all the unknowns mentioned.

Being the largest mass objects, it is reasonable to assume that the objects observed in the two redshift intervals represent the population that will eventually become the most massive BHs in the most massive galaxies in the local universe. As explained in Netzer et al. (2014), this is likely but by no means the only possibility. Netzer et al. (2014) considered various possibilities regarding the location of the host galaxies of the most luminous AGNs at $z \simeq 4.8$ relative to the MS at that redshift. The discussion included various scenarios, such as strong and moderate feedback, the accumulation of stellar and BH mass under various growth modes (exponential and linear growth), and the required duty cycles to explain the observations available at that time. We do not repeat this analysis, partly because all the details are given in Netzer et al. (2014), and partly because of the lack of BH mass measurements at $z = 2$–3.5. Instead, we briefly report on those scenarios that are consistent with the new observations, and point out some tests that can be done to verify these ideas.

For simplicity, we consider BH growth during 1 Gyr between $z \simeq 4.8$ and $z \simeq 2.9$, taking the latter to represent our $z = 2$–3.5 sample (the median redshift of our current sample is somewhat lower, about 2.6). The mean $L_{\rm AGN}$ over this period translates to BHAR $\sim 8\,M_{\odot}\,{\rm yr}^{-1}$. Therefore, accumulating the additional BH mass (an increase by a factor 4 growing from $10^{8.9}$ to $10^{9.5} M_{\odot}$) requires a linear growth with a duty cycle of approximately 0.5. For exponential growth, the duty cycle is shorter.

For the stellar-mass growth, we assume that at $z \simeq 4.8$ the host galaxy mass is in the range $10^{11-11.5}\ M_{\odot}$. According to Schreiber et al. (2015), at $z \simeq 4.8$ the SFR for a $10^{11}\,M_{\odot}$ MS galaxy is about 260 $M_{\odot}\,{\rm yr}^{-1}$ and for a $10^{11.5}\,M_{\odot}$ MS galaxy it is about 790 $M_{\odot}\,{\rm yr}^{-1}$. The corresponding numbers at $z \simeq 2.9$ are about 140 and 330 $M_{\odot}\,{\rm yr}^{-1}$, respectively. Assuming we are following the same population in time, it is reasonable to suggest that the lowest stellar mass to consider at $z = 2$–3.5 is $10^{11.5} M_{\odot}$. Using these stellar-mass estimates, and assuming a typical MS width of ±0.3 dex, we suggest that most of the *Herschel*-detected sources at $z \simeq 4.8$ are above the MS and most of the undetected sources at that redshift are on the MS. As for the $z = 2$–3.5 sample, the median SFR for the stacked sources is roughly 100 $M_{\odot}\,{\rm yr}^{-1}$ (Table 4), which means that most or perhaps all objects with stellar mass of $10^{11.5}\,M_{\odot}$ or larger are below the MS. This is consistent with the assumption that all the *Herschel*-undetected sources at $z = 2$–3.5 (i.e., about 2/3 of the objects in our sample) are quenching or possibly quenched galaxies. Obviously the distribution in SFR for undetected sources is likely to be wide and the information that we have is only about the mean and median properties of the population. We did not consider SF hosts with stellar masses smaller than $10^{11}\,M_{\odot}$ at $z = 2$–3.5, which is probably unphysical given the very large BH mass expected in these very luminous AGNs.

Given all these numbers, a stellar-mass growth at a rate of $10^{3}\,M_{\odot}\,{\rm yr}^{-1}$ starting at $z \simeq 4.8$ gives just enough time to accumulate mass that, at $z = 2$–3.5, is similar to the mass of the most massive galaxies of today. The estimate is basically independent of the starting stellar mass. This scenario is consistent with known stellar-mass functions at the same redshift range (Ilbert et al. 2013; Madau & Dickinson 2014), provided a complete quenching occurs toward the end of this redshift interval. Faster stellar-mass growth, which is more consistent with the sSFR of the *Herschel*-detected sources at $z \simeq 4.8$, requires less time, with a duty cycle of the order of 0.2, or quenching at redshift larger than 3.5, consistent with ideas about the epoch of the fastest growth of the most massive galaxies of today.

Regarding undetected sources, and assuming that we observe the same population at both redshifts, most such objects are still on the MS at $z \simeq 4.8$ but below the MS at $z = 2$–3.5. Either the hosts of these BHs are low mass SF galaxies, which is problematic given the assumed very large BHs at $z \simeq 4.8$, or else quenching becomes important between these two epochs. If the latter is correct, then the active BHs we observe in this group are consuming the remaining gas near the center while SF in the galaxy has ceased. These BHs may be on their way to becoming the most massive BH known. A similar phase may occur at redshift smaller than 2 for those sources that are still forming stars at high rate at $z = 2$–3.5.

It is interesting to note that the scenario described for *Herschel*-detected sources at $z \simeq 4.8$ and $z = 2$–3.5, which identifies them as the most massive systems of today, is also consistent with the measured SFR/BHAR. In most of these sources, $L_{\rm SF} \sim L_{\rm AGN}$. For this luminosity ratio, SFR/BHAR ∼ 140 (Netzer et al. 2014), which is a ratio that is very close to the stellar-to-BH mass ratio observed in the spheroidal galaxies hosting the most massive BHs at $z = 0$.

[7] Note that the Eddington ratio in this sample is considerably below 1, while the typical values at $z \simeq 4.8$ are significantly higher.

[8] The median BH mass for the *Herschel*-detected sources at $z \approx 4.8$ is $10^{8.9}\,M_{\odot}$.

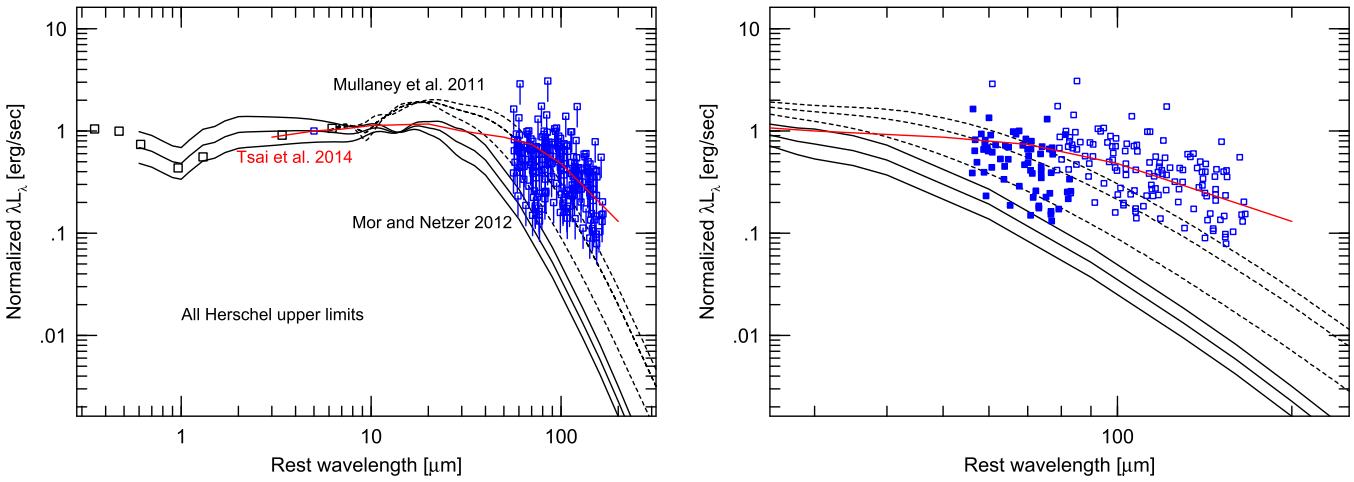

Figure 7. Left: the shape of the torus SED from FIR upper limits. The diagram shows all *Herschel*/SPIRE upper limits for the undetected sources in our sample normalized to $L_{5\mu m}$ derived from the *WISE* data. The short wavelength points show the NIR-*WISE* data of a representative object (HE-2156-4020 at $z = 2.531$). The central solid black line is the Mor & Netzer (2012) SED used throughout the paper and the two other solid lines are the 25% and 75% limits discussed in that paper. The dashed black lines are the three SEDs suggested by Mullaney et al. (2011) normalized to the Mor & Netzer (2012) SED at 6 μm; from top to bottom: high-L, mean, and low-L sources. The SPIRE upper limits indicate that if all sources have the same SED, they cannot exceed the Mor & Netzer (2012) template by more than approximately 10% at rest-frame wavelengths of 60–90 μm. The red line is the Tsai et al. (2015) torus SED normalized to the observed 5 μm continuum. Right: zoom in on the long wavelength part (error bars removed for clarity). The full squares mark the 250 μm upper limits.

Finally, the suggestion that the *Herschel*-detected sources at $z \simeq 4.8$ and $z = 2$–3.5 represent the same population, puts a question mark on the idea that AGN feedback in such sources is an important process that regulates their stellar-mass growth. Such extremely luminous AGNs are active, for a long period of time, without affecting the very fast SF in their host galaxies.

3.4. Torus Properties: SED and Covering Factor

3.4.1. Constraints on the Torus SED

The observations presented here can be used to obtain information about several of the nuclear components in the objects under study. In particular, we can set limits on the shape of the torus SED in highly luminous sources, thus improving the estimates of the total dust emission by the torus, and estimate more accurately its covering factor (C_f). We can also look for signs of intrinsic reddening due to interstellar or circumnuclear dust in the host galaxy.

Constraints on the short wavelength part of the torus spectrum can be obtained from a study of the data presented in Figure 3. Interestingly, detected and undetected *Herschel* sources display remarkably similar shapes over the 1–10 μm range that are all consistent with the median SED of Mor & Netzer (2012). The long wavelength part of the torus spectrum is more difficult to observe due to contamination by SF in the host galaxy. This part is best studied by using SPIRE upper limits. We tested several different suggested torus SEDs. The first is the Mor & Netzer (2012) template used throughout this paper, where the turning down (in λL_λ) is at wavelengths greater than $\sim$25 μm. The second is a set of three SEDs published by Mullaney et al. (2011; listed in their Table 3). All three are flat, in λL_λ, up to 30–40 μm and drop down, in a luminosity-dependent way, beyond this wavelength. The final SED is the one used by Tsai et al. (2015), partly in attempt to fit the global spectrum of highly obscured, luminous AGNs. This template was adapted from the earlier works of Polletta et al. (2006) and Polletta et al. (2007). It is similar to the Mor & Netzer (2012) SEDs at short wavelengths, but extends to longer wavelengths with a drop starting at around 50 μm. The main difference between the Tsai et al. (2015) SED compared to the Mor & Netzer (2012) and Mullaney et al. (2011) SEDs is that the former do not take into account the SF contribution at FIR wavelengths.

The stack spectrum shown in Figure 3 provides strong constraints on the torus SED and demonstrates that it cannot exceed the Mor & Netzer (2012) SED by a large amount at rest-wavelengths of 60–90 μm because the flux emitted by the torus cannot exceed the stacked fluxes. Individual SPIRE upper limits (i.e., three times the confusion limits) provide even stronger constraints. This is illustrated in Figure 7, which shows the Mor & Netzer (2012) SEDs (composite and upper and lower limits), the three Mullaney et al. (2011) SEDs, and the Tsai et al. (2015) SED all normalized to our median observed SED at 5–6 μm. The left panel of the diagram shows the 3σ upper limits in the three SPIRE bands for the 66 undetected sources in our sample, and the right panel zooms in on the more important part of the diagram. While we cannot exclude the possibility that the torus SED changes from one source to the next, we can put strong constraints on its shape under two simplified assumptions. The first assumption is that all sources have the same torus SED within the 25%–75% range set by Mor & Netzer (2012). The diagram shows that all our sources are consistent with this assumption. The high-L SED of Mullaney et al. (2011) is consistent with most but not all objects.

Alternatively, we can test the assumption that the Mullaney et al. (2011) SEDs, or the Tsai et al. (2015) SED, provide good fits to the undetected sources by comparing their predicted $250/(1 + z)$ μm luminosity to the observations. For the high-L Mullaney et al. (2011) SED, we find that 24% of the undetected *Herschel* sources would have been detected by SPIRE at a 3σ level if this was, indeed, the torus SED. For the mean Mullaney et al. (2011) SED, this number is 71% and for the Tsai et al. (2015) SED it is 85%. These tests suggest that the Mor & Netzer (2012) SED is the best choice for our sample and and some of the alternative SEDs tried here are less consistent with

the observations. This justifies our earlier assumption that, except for the weak-NIR sources, simple integration over the chosen SED is appropriate for estimating the torus covering factor in our sample.

3.4.2. Intrinsic Reddening

We also considered the possibility of intrinsic reddening in our sources. For this we need to compare the estimated $L_{\rm AGN}$, which can be affected by reddening, and $L_{\rm torus}$, which is independent of reddening. Our comparison is based on the torus SED adopted here, which fits well all the sources except for the weak-NIR AGNs, where it clearly overestimates $L_{\rm torus}$. We have 12 weak-NIR sources that represent 12% of our sample and are very similar to their fraction in the general population (e.g., Mor & Trakhtenbrot 2011; Roseboom et al. 2013). The correlations and diagrams described in the following do not include these sources.[9]

Intrinsic reddening is hard to check in individual sources because of the large scatter in the intrinsic shape of the optical-UV continuum (e.g., Krawczyk et al. 2013, 2015 and references therein). Lusso et al. (2013) discussed $z = 0$–5 AGNs and assumed a single disk-like SED adopted from an observed composite by Richards et al. (2006). The normalization of the SED is based on the multi-band photometry of their sources. They find that 24% of the sources in their sample are affected by significant reddening corresponding to $\langle E(B-V)\rangle = 0.1$ mag, where the sample mean is $\langle E(B-V)\rangle = 0.03$ mag. One major limitation of this method is the assumption that the SED of the accretion disk, assumed to be the central powerhouse, is independent of the source luminosity and BH mass, and the bolometric luminosity is independent of the disk inclination to the line of sight. This assumption is in contrast with calculated thin disk SEDs that depend on BH mass, BHAR, and BH spin (e.g., Capellupo et al. 2015 and references therein).

We chose not to make specific assumptions about the origin of the intrinsic AGN SED, but rather to look for significant variations in continuum slope as reddening indicators. For this we compared the rest-frame L_{1350}, and the luminosity derived from the K-band flux, which is available for about half the sources in our sample. We used these measurements to derive the continuum slope, α, between the two wavelengths. The K-band central wavelength corresponds to rest-frame wavelengths between 0.49 and 0.73 μm, depending on the redshift. Given the rough nature of this comparison, we did not take into account the contribution to the K-band flux from Hβ and FeII lines in objects with $z > 3$, and the contribution from Hα in sources at $z \sim 2$. The distribution in α calculated in this way, assuming $L_\nu \propto \nu^{-\alpha}$, is broad with α in the range 0–1, and resembles the general distribution in large samples of unreddened AGNs (Krawczyk et al. 2015). The median slope for the entire sample can be found by comparing the median IR SED, extended to below 1 μm, and the median L_{1350}. This slope is $\alpha = 0.22$, which again is similar to what is found in large AGN samples. We find no correlation of slope with $L_{5\mu{\rm m}}/L_{1350}$ and, therefore, neglect the effect of intrinsic reddening on $L_{\rm torus}/L_{\rm AGN}$ in our sample. Note that such information is only available for about half the sources in our sample.

[9] Both Roseboom et al. (2013) and Leipski et al. (2014) use individual torus model for every source and so their measured $L_{\rm torus}$ represent well the total dust emission by the torus.

Figure 8 shows $L_{\rm torus}/L_{\rm AGN}$ as a function of $L_{\rm AGN}$ for all sources in our sample except the 12 weak-NIR sources whose $L_{\rm torus}$ is more uncertain. We calculated the ratio under the two different assumptions considered earlier for the bolometric correction factor: ${\rm Bol}_{1350} = 2$ in the left panel and ${\rm Bol}_{1350} = (49 - \log L_{1350})$ in the right panel. A regression analysis using the BCES method gives, in the first case, a marginally significant slope of -0.46 ± 0.27, and in the second case a slope that is consistent with no correlation (-0.35 ± 0.86). Thus the uncertainty in $L_{\rm AGN}$ due to the large possible range in ${\rm Bol}_{1350}$) completely masks any real dependence of $L_{\rm torus}/L_{\rm AGN}$ on $L_{\rm AGN}$. We also show (small black points) similar data for the partial Shen et al. (2011) log L_{1350} (erg s^{-1}) > 46.5 sample discussed in Section 2.5. The dependence of $L_{\rm torus}/L_{\rm AGN}$ on $L_{\rm AGN}$ is similar and the conclusions are unchanged. We investigate this issue using results from several other samples in the following section.

3.4.3. Covering Factor

Next we consider the geometrical covering factor of the torus, C_f. For this we need to consider possible anisotropies in $L_{\rm torus}$, $L_{\rm AGN}$, and their ratio. The first source of anisotropy is the geometry of the central powerhouse, considered here to be an optically thick, geometrically thin or slim accretion disk. For thin disks, the angular dependence of the emitted radiation, neglecting general relativistic effects at very high frequencies, is wavelength independent and varies roughly as $\cos i$, or $\cos i(1 + a\cos i)$, where i is the inclination angle and $a \approx 2$ (e.g., Netzer 2013). For a thin disk whose axis is parallel to that of the torus in a type-I AGN, this factor is in the range 0.5–1, representing the range of inclinations from zero to 60°. The expected anisotropy in slim accretion disks is much larger (Wang et al. 2014 and references threin). The calculations of the SED, in this case, are far more complicated and therefore highly uncertain.

The second source of anisotropy is the dusty torus itself. The radiation pattern of such tori have been discussed extensively in the literature (e.g., Nenkova et al. 2008b; Stalevski et al. 2012 and references therein) and reviewed recently by Netzer (2015). Strong anisotropy, especially at short wavelength where the dust optical depth is the largest, is predicted by most torus models. The exact angular dependence differs substantially from one model to the next, partly because of the different geometries used in such calculations. For example, a new work by M. Stalevski (2015, private communication) suggests that for both continuous and composite clumpy tori, the torus is very difficult to detect for very small C_f because of the inner disk anisotropy, and the relation between $L_{\rm torus}/L_{\rm AGN}$ and C_f is nonlinear at large covering factors.

Given the large uncertainties, we decided to adopt the simple anisotropy correction factor of Netzer (2015), which is similar to those used by Treister et al. (2008) and Lusso et al. (2013). (Roseboom et al. 2013 did not apply an anisotropy correction factor and their results refer to the case of complete isotropy.) For this we introduce an isotropy parameter, b, that can vary between 1 (complete isotropy; i.e., the part of the radiation emitted into the torus opening is proportional to the solid angle of the opening in the torus) and 0 (complete anisotropy; all torus emission is emitted into the opening). In this case,

$$\frac{L_{\rm torus}}{L_{\rm AGN}} = \frac{1 - bC_f}{1 - C_f} C_f. \quad (3)$$

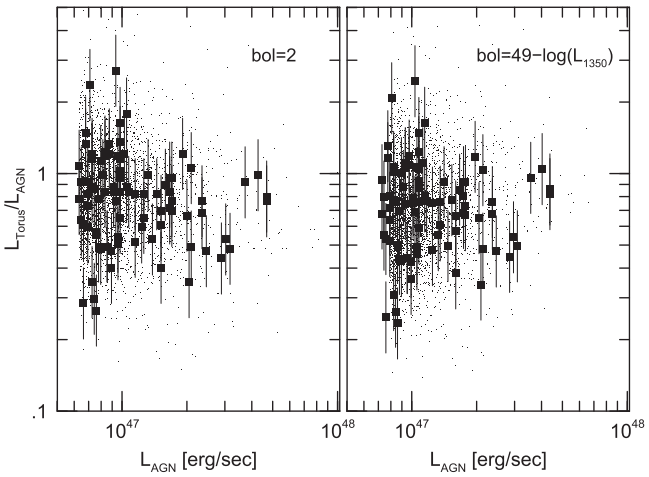

Figure 8. $L_{\rm torus}/L_{\rm AGN}$ for the $z = 2$–3.5 sample, excluding weak-NIR sources (large symbols), and the comparable Shen et al. (2011) sample (small points). The two panels illustrate the changes resulting from the use of different bolometric correction factors (marked in the diagram as "bol").

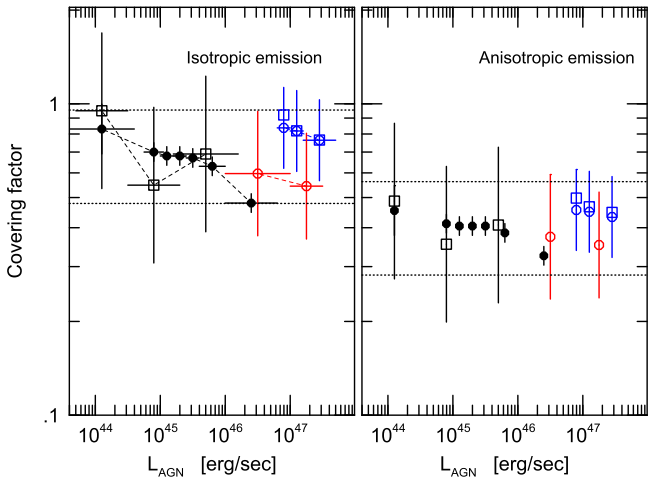

Figure 9. Covering factor as a function of $L_{\rm AGN}$ in large AGN samples. Open black squares: the Mor & Netzer (2012) sample. Full black circles: the Lusso et al. (2013) sample. Open red circles: the Roseboom et al. (2013) sample. Open blue circles: the the present $z = 2$–3.5 sample without the weak-NIR sources. Open blue squares: SDSS sources from the Shen et al. (2011) catalog with the same redshift and luminosity as the present sample and $L_{5\mu\rm m}$ measured as explained in the text. The left panel shows the covering factors under the assumption of isotropic dust emission. As explained in the text, the Roseboom et al. (2013) values are scaled up by factors of 1.5–1.8 to allow for the different assumed bolometric correction factors. The parallel dotted lines show the range of ± 0.15 dex around the mean value of 0.68. The right panel shows the same data for the case of complete anisotropy ($b = 0$ in Equation (3)). The dotted lines indicate a range of ± 0.15 dex around 0.4.

This expression does not take into account anisotropic disk emission that affects $L_{\rm AGN}$ and is equivalent to the assumptions of the same disk inclination angles in all type-I AGNs. It does not necessarily increase the uncertainty because if the disk and the torus axes are aligned, the ratio $L_{\rm torus}/L_{\rm AGN}$ depends less on inclination to the line of sight.

The parameter b depends on the optical depth of the dust in the torus and is therefore wavelength dependent. The dependence affects the conversion between the observed $L_{\rm torus}$ and the total dust emission, as well as the scaling of the total dust emission relative to the measured $L_{5\mu\rm m}$ (i.e., the factor of 3.58 introduced in Section 2.5). For the extreme cases of very small optical depth (complete isotropy) or large optical depth over the entire 2–20 μm range, this dependence will not affect the derived covering factor. Here we neglect the wavelength dependence of b.

We compiled from the literature a large number of estimated covering factors based on NIR–MIR observations. They include (1) the COSMOS sample of Lusso et al. (2013); here we take median data shown in Figure 12 of their paper. (2) The Roseboom et al. (2013) *WISE*-based $z \leqslant 1.5$ sample; here we take the mean and standard deviations from their Figure 4, but make an adjustment to correct for the fact that their bolometric correction factors obtained from Shen et al. (2011) are significantly larger than those in our work (Section 2.6). This adjustment results in a considerable increase in the mean $L_{\rm torus}/L_{\rm AGN}$. (3) The Mor & Netzer (2012) sample; this sample includes ~100 low-to-intermediate luminosity objects collected from the literature, including many narrow-line Seyfert 1 galaxies and QUEST QSOs. We used the observed L_{5100} to obtain $L_{\rm AGN}$ and $L_{5\mu\rm m}$ to obtain $L_{\rm torus}$. We did not use the estimated covering factors listed in their paper, which were based on the specific anisotropy provide by the Nenkova et al. (2008a) model because this is a model-dependent way that is completely different from the method used for obtaining C_f in the other samples.

Several other samples use NIR–MIR observations to calculate covering factors. In particular, Treister et al. (2008) present covering factor estimates based on flux measured in a single *Spitzer* band (24 μm). They made several assumptions about the total torus emission and calculated $L_{\rm AGN}$ in a way that is somewhat different from what we used here. Intriguingly, their estimated $L_{\rm torus}/L_{\rm AGN}$ is significantly larger than what was obtained by others for a similar range of luminosity and redshift. The discrepancy was discussed by Lusso et al. (2013) without a real resolution. We decided not to consider this sample because the redshift and luminosity ranges are nicely covered by other samples where $L_{\rm torus}$ is better defined. The Maiolino et al. (2007) multi-redshift sample used *Spitzer*-IRS data to constrain the torus SED. This sample was discussed in great detail by Lusso et al. (2013), who showed a very good agreement with their results. Thus the data we present here represent well the results of Maiolino et al. (2007).

Figure 9 shows all the NIR–MIR-based compilations of C_f, including ours, for the case of complete isotropic dust emission ($b = 1$) on the left, and maximum anisotropy ($b = 0$) on the right. For the present sample, we only show the case of $\rm Bol_{1350} = 2$. The uncertainty on $L_{\rm AGN}$ represents the range in this property that is used to derive the median values. The uncertainty on $L_{\rm torus}/L_{\rm AGN}$ is taken from the original papers (Lusso et al. 2013; Roseboom et al. 2013) or from the present calculations. Given the uncertainties on $L_{\rm torus}$ and $L_{\rm AGN}$, we estimate a combined uncertainty on C_f of at least ± 0.2 dex at all $L_{\rm AGN}$. We also show, as blue open squares, the median values obtained from Shen et al. (2011) and shown in Figure 8 left panel ($\rm Bol_{1350} = 2$).

The diagrams presented here show that all medians of all the samples used here, at all $L_{\rm AGN}$, are confined to a band of width ± 0.15 dex in $L_{\rm torus}/L_{\rm AGN}$ around 0.68 for the isotropic case, and 0.4 for the case of complete anisotropy. Because much of the uncertainty in C_f is systematic and depends on the poorly known bolometric correction factor, the inclusion of a large number of individual measurements cannot improve the situation by much. Thus, the torus covering factors that are based on NIR–MIR measurements show no indication for a decrease of C_f with increasing source luminosity. This finding

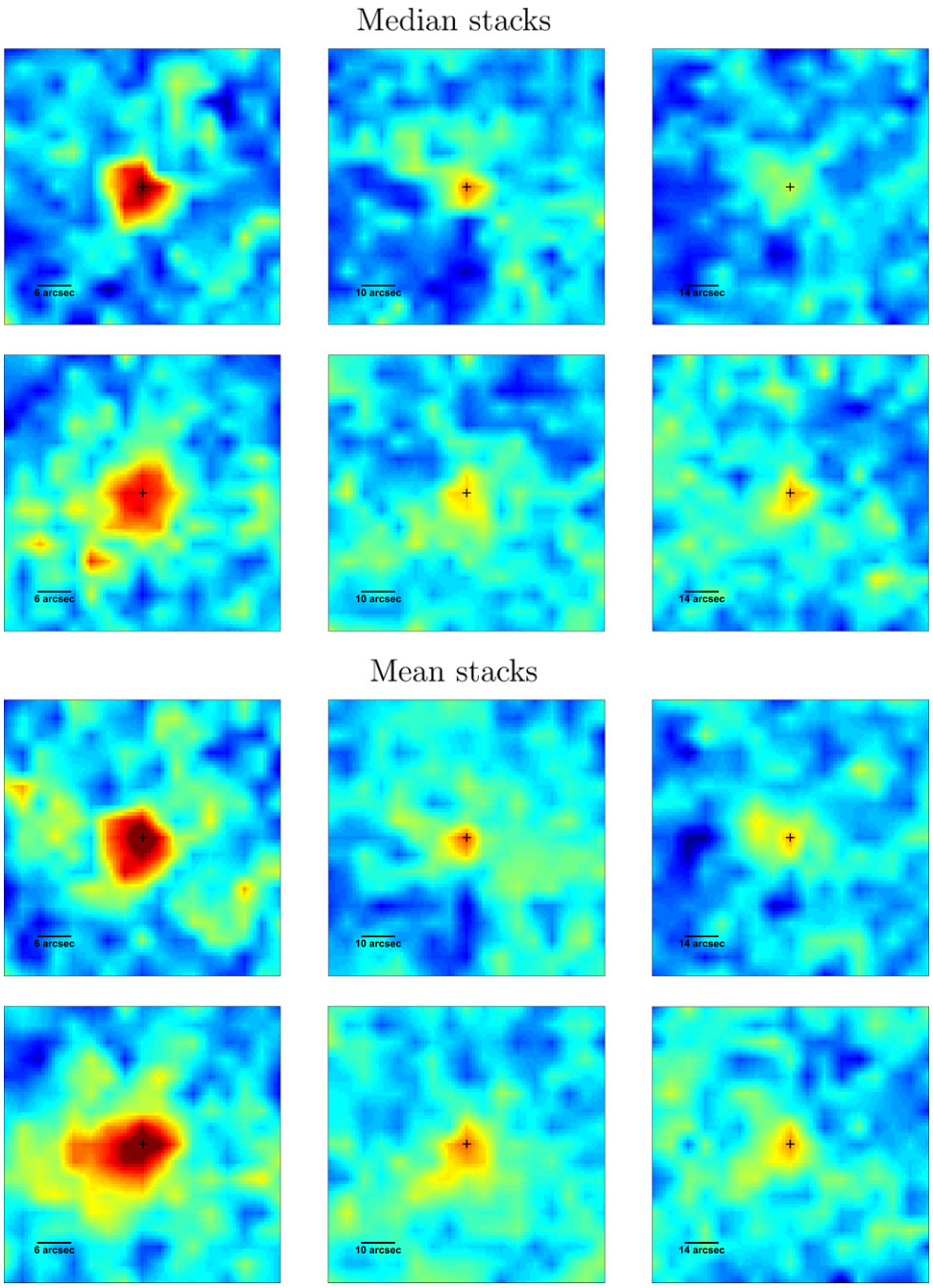

Figure 10. Median (top) and mean stacks. In each part, the high luminosity group is shown in the upper row and the low luminosity group in the lower row. From left to right: 250, 350, and 500 μm. The crosses mark the centers of the stacks.

seems to contradict earlier findings, such as those presented by Lusso et al. (2013) and Roseboom et al. (2013).

An independent way of estimating the covering factor is to compare the fraction of type-II AGNs in the AGN population as a function of redshift and luminosity, either by searching for X-ray obscuration or by counting sources in large optical surveys. This has been an active area of research for many years and was investigated in numerous X-ray papers (e.g., Steffen et al. 2003; Ikeda et al. 2009; Yaqoob et al. 2010; Brightman & Nandra 2011; Ricci et al. 2013; Buchner et al. 2015). A additional way is to compare type-I and type-II LFs (Simpson 2005). A detailed comparison of X-ray derived and IR-derived covering factors is beyond the scope of the present paper. We only point out that disagreements between the various methods have been noted in earlier works, especially for low luminosity AGNs, and are partly due to the different cut-offs in column density that are adopted in different papers (see a comprehensive discussion in a recent paper by Merloni et al. 2014). There are still fundamental unresolved issues related to the relative fraction of type-I and type-II sources at different luminosity and redshift. One such difficulty is related to the "true" type-II AGNs found in low luminosity samples. Another uncertainty is related to the difficult-to-detect broad wings in low luminosity type-I sources (Oh et al. 2015). A good example of a difficulty of assessing the covering factor in X-ray samples is the recent work by Vito et al. (2014) that

classifies AGNs into groups based on the line-of-sight absorbing column of 10^{23} cm^{-2}, which is considerably larger than the column densities used in earlier studies. This work suggests a roughly 1:1 ratio of type-I and type-II AGNs over a large range of X-ray luminosity, which overlaps, given standard bolometric correction factors, with the luminosities in our sample. This would indicate $C_f \sim 0.5$. A comprehensive review of many of these issues is given in Netzer (2015).

The above finding questions the validity of the "receding torus" model suggested by Lawrence (1991) and discussed in numerous other papers. The model aims at explaining the seemingly decreasing covering factor of AGN tori as a function of $L_{\rm AGN}$. It is based on observational and theoretical ideas that the innermost boundary of the central dusty torus is defined by the dust sublimation radius (e.g., Barvainis 1987; Netzer & Laor 1993). Recent studies (Koshida et al. 2014 and references therein) based on dust reverberation mapping show the good agreement between the dust innermost location and the sublimation radius of pure graphite dust (Mor & Netzer 2012). In particular, they show a clear dependence of the the innermost dust location on $L_{\rm AGN}{}^{1/2}$, as expected in the simplest model of this type. The receding torus idea takes this idea one step further by assuming that the vertical scale of the torus (the torus "height") is independent, or only weakly dependent, on source luminosity. This assumption results in a smaller covering factor for larger $L_{\rm AGN}$. There is little if any theoretical justification of this idea.

The present work suggests that, given the uncertainties, the covering factors of tori in the most luminous AGNs may be very similar to those in sources that are three orders of magnitude less luminous. For the simple torus models this is equivalent to a factor of ∼30 in distance between the central BH and the torus inner walls. We suggest that earlier claims to the contrary could be biased mostly by the inconsistent use of various bolometric correction factors and that the overall geometry (shape and size) of the AGN tori scale in accord with the bolometric luminosity. The evidence presented here is based on intermediate to high luminosity AGNs (see luminosity scale in Figure 9) and hence does not apply to lower luminosity AGNs in the local universe. A future, more detailed study of the covering factor distribution as a function of $L_{\rm AGN}$ must be limited to a narrow redshift range to avoid evolutionary biases.

4. CONCLUSIONS

The *Herschel*/SPIRE observations reported here provide new information about 100 very luminous, optically selected type-I AGNs at $z = 2$–3.5 with log $L_{\rm AGN}$ (erg s^{-1}) $\geqslant 46.8$, assuming $L_{\rm AGN} = 2\ L_{1350}$. Our sample provides the most complete information, in terms of numbers, about this population because there are very few such objects in other *Herschel*-selected fields. The distribution in L_{1350} and $L_{5\mu\rm m}$ of the sources is similar to the distribution in the general population (SDSS), and we can use the sample to study several outstanding problems related to SF and BH activity in such sources. In particular, we can combine the sample with two previous studies at high redshift—those of Netzer et al. (2014) and Leipski et al. (2014)—and follow BHAR and SFR and their ratio over the redshift interval 2–7, albeit with incomplete information for the $z > 5$ population. The main results are:

1. Of the 100 sources, 34 are detected by *Herschel* at the 3σ level. For the undetected sources, we present two statistically significant stacks representing sources in two luminosity groups: log L_{1350} (erg s^{-1}) = 46.5–46.7 and log L_{1350} (erg s^{-1}) > 46.7. The mean and the median SFRs of the detected sources are 1176^{+476}_{-339} and 1010^{+706}_{-503} $M_\odot$ yr^{-1}, respectively. The mean SFR of the undetected sources is 148 $M_\odot$ yr^{-1}. (The uncertainty is not given because we did not stack the entire group of undetected sources; see Table 4 for more information.) Unlike our earlier $z \simeq 4.8$ sample, the $z = 2$–3.5 sources do not show significant differences in $L_{\rm AGN}$ and $L_{\rm torus}$ between *Herschel*-detected and undetected sources.
2. The combination of the three high-redshift samples show that the redshift distribution of $L_{\rm SF}$ and $L_{\rm AGN}$ for the most luminous, redshift 2–7 AGNs are different. Like the entire SDSS sample, the highest $L_{\rm AGN}$ increases with decreasing redshift, peaking at $z \approx 3$. However, the highest $L_{\rm SF}$ in the host galaxies of the most luminous AGNs increases with decreasing redshift more rapidly, and peaks at $z \approx 5$. Assuming the objects in our sample are hosted by the most massive galaxies at $z = 2$–3.5, we argue that some 30% of the hosts are on and above the MS, and most of the remaining 70% are below the MS. The ratio of the stellar-to-BH mass growth rate is ≈80 in the high SFR, *Herschel*-detected sources, and less than 10 in the group of low SFR galaxies.
3. The shapes of the SEDs of the dusty tori in our sample, as derived from a combination of *WISE* and J,H,K photometry, are very similar to the shapes found in low redshift, low luminosity AGNs. The measured *Herschel* upper limits put strong constraints on the long wavelength part of this SED. The upper limits are in good agreement with the Mor & Netzer (2012) composite torus SED, in somewhat worse agreement with the high-L and mean Mullaney et al. (2011) SEDs, and in contradiction with the Tsai et al. (2015) SED where the turning down is at very long wavelengths.
4. Combining our results at $z = 2$–3.5 with those of several earlier studies, and correcting for biases due to different bolometric correction factors used in the earlier works, we find no evidence for a luminosity dependence of the torus covering factor in sources with log $L_{\rm AGN}$ (erg s^{-1}) = 44−47.5. This conclusion is based on various assumptions, mostly the recognition of the large uncertainties in several earlier calculations of $L_{\rm AGN}$. The median covering factors over this range are 0.68 for isotropic dust emission and 0.4 for anisotropic emission, with an uncertainty of 0.15 dex on both numbers.

We thank the anonymous referee for providing numerous suggestions that helped to improve the presentation of the paper. This work is based on observations made with *Herschel*, a European Space Agency Cornerstone Mission with significant participation by NASA. The Herschel-ATLAS is a project with Herschel, which is an ESA space observatory with science instruments provided by European-led Principal Investigator consortia and with important participation from NASA. The H-ATLAS website is http://www.h-atlas.org/. This research has made use of data from HerMES project (http://hermes.sussex.ac.uk/). HerMES is a *Herschel* Key Programme utilizing Guaranteed Time from the SPIRE instrument team, ESAC scientists, and a mission scientist. The HerMES data was accessed through the *Herschel* Database in Marseilles (HeDaM—*http://hedam.lam.fr*)

operated by CeSAM and hosted by the Laboratoire d'Astrophysique de Marseilles. Support for this work was provided by NASA through an award issued by JPL/Caltech. Funding for this work has been provided by the Israel Science Foundation grant 284/13.

APPENDIX

This appendix contains the scan IDs of the HerMES fields relevant to this work in Table 5. When searching for detections in the large surveys we considered the catalogs found in Table 6.

Table 5
Scan IDs of the HerMES Fields Relevant to This Work

HerMES Field	*Scan IDs*
Lockman-North	1342186110, 1342222588, 1342222589, 1342222590, 1342222591, 1342222593, 1342222594 1342222595, 1342222596
Lockman-Swire	1342186108, 1342186109, 1342222588, 1342222589, 1342222590, 1342222591, 1342222593, 1342222594, 1342222595, 1342222596
GOODS-North	1342185536
Böotes	1342187711, 1342187712, 1342187713, 1342188090, 1342188650, 1342188651, 1342188681, 1342188682, 1342189108
ELAIS-N1	1342187646, 1342187647, 1342187648, 1342187649, 1342187650

Table 6
Catalogs Considered when Searching for Detections in Large Surveys

Survey Field	*Catalog Name*	*Web Link*
HerS	hers_catalogue_3-sig250_no_extended.fits	http://www.astro.caltech.edu/hers/Data_Product_Download.html
H-Atlas SDP	HATLAS_SDP_catalogue.fits	http://www.h-atlas.org/public-data/download
HerMES Lockman-North	L3-Lockman-North_-xID250_DR2.fits.gz L3-Lockman-North_-xID350_DR2.fits.gz L3-Lockman-North_-xID500_DR2.fits.gz	http://hedam.lam.fr/HerMES/index/all_files
HerMES Lockman-Swire	L5-Lockman-SWIRE_SCAT250SXT_DR2.fits.gz L5-Lockman-SWIRE_SCAT350SXT_DR2.fits.gz L5-Lockman-SWIRE_SCAT500SXT_DR2.fits.gz	http://hedam.lam.fr/HerMES/index/all_files
HerMES GOODS-North	L2-GOODS-North_-SCAT250SXT_DR2.fits.gz L2-GOODS-North_-SCAT350SXT_DR2.fits.gz L2-GOODS-North_-SCAT500SXT_DR2.fits.gz	http://hedam.lam.fr/HerMES/index/all_files
HerMES Böotes	L5-Bootes-HerMES_S-CAT250SXT_DR2.fits.gz L5-Bootes-HerMES_S-CAT350SXT_DR2.fits.gz L5-Bootes-HerMES_S-CAT500SXT_DR2.fits.gz	http://hedam.lam.fr/HerMES/index/all_files
HerMES ELAIS-N1	L5-ELAIS-N1-HerMES_S-CAT250_DR2.fits.gz L5-ELAIS-N1-HerMES_S-CAT350_DR2.fits.gz L5-ELAIS-N1-HerMES_S-CAT500_DR2.fits.gz	http://hedam.lam.fr/HerMES/index/all_files

REFERENCES

Abazajian, K. N., Adelman-McCarthy, J. K., Agüeros, M. A., et al. 2009, ApJS, 182, 543
Adelman-McCarthy, J. K., Agüeros, M. A., Allam, S. S., et al. 2007, ApJS, 172, 634
Antonucci, R. 1993, ARA&A, 31, 473
Assef, R. J., Stern, D., Kochanek, C. S., et al. 2013, ApJ, 772, 26
Barvainis, R. 1987, ApJ, 320, 537
Béthermin, M., Dole, H., Beelen, A., & Aussel, H. 2010, A&A, 512, A78
Brightman, M., & Nandra, K. 2011, MNRAS, 413, 1206
Buchner, J., Georgakakis, A., Nandra, K., et al. 2015, ApJ, 802, 89
Capellupo, D. M., Netzer, H., Lira, P., Trakhtenbrot, B., & Mejía-Restrepo, J. 2015, MNRAS, 446, 3427
Castignani, G., & De Zotti, G. 2015, A&A, 573, A125
Chabrier, G. 2003, PASP, 115, 763
Chary, R., & Elbaz, D. 2001, ApJ, 556, 562
Chen, C.-T. J., Hickox, R. C., Alberts, S., et al. 2013, ApJ, 773, 3
Croom, S. M., Richards, G. T., Shanks, T., et al. 2009, MNRAS, 399, 1755
Daddi, E., Alexander, D. M., Dickinson, M., et al. 2007, ApJ, 670, 173
Davis, M., Guhathakurta, P., Konidaris, N. P., et al. 2007, ApJL, 660, L1
Delvecchio, I., Lutz, D., Berta, S., et al. 2015, MNRAS, 449, 373
Dole, H., Lagache, G., Puget, J.-L., et al. 2006, A&A, 451, 417
Drouart, G., De Breuck, C., Vernet, J., et al. 2014, A&A, 566, A53
Eales, S., Dunne, L., Clements, D., et al. 2010, PASP, 122, 499
Griffin, M. J., Abergel, A., Abreu, A., et al. 2010, A&A, 518, L3
Gruppioni, C., Pozzi, F., Rodighiero, G., et al. 2013, MNRAS, 432, 23
Harrison, C. M., Alexander, D. M., Mullaney, J. R., et al. 2012, ApJL, 760, L15
Hatziminaoglou, E., Omont, A., Stevens, J. A., et al. 2010, A&A, 518, L33
Hickox, R. C., Mullaney, J. R., Alexander, D. M., et al. 2014, ApJ, 782, 9
Ikeda, S., Awaki, H., & Terashima, Y. 2009, ApJ, 692, 608
Ilbert, O., McCracken, H. J., Le Fèvre, O., et al. 2013, A&A, 556, A55
Jannuzi, B. T., Dey, A., Brown, M. J. I., et al. 2004, BAAS, 36, 1478
Kormendy, J., & Ho, L. C. 2013, ARA&A, 51, 511
Koshida, S., Minezaki, T., Yoshii, Y., et al. 2014, ApJ, 788, 159
Krawczyk, C. M., Richards, G. T., Gallagher, S. C., et al. 2015, AJ, 149, 203
Krawczyk, C. M., Richards, G. T., Mehta, S. S., et al. 2013, ApJS, 206, 4
Lawrence, A. 1991, MNRAS, 252, 586
Leipski, C., Meisenheimer, K., Walter, F., et al. 2014, ApJ, 785, 154
Lira, P., Videla, L., Wu, Y., et al. 2013, ApJ, 764, 159
Lonsdale, C. J., Smith, H. E., Rowan-Robinson, M., et al. 2003, PASP, 115, 897
Lusso, E., Hennawi, J. F., Comastri, A., et al. 2013, ApJ, 777, 86
Madau, P., & Dickinson, M. 2014, ARA&A, 52, 415
Mainieri, V., Bongiorno, A., Merloni, A., et al. 2011, A&A, 535, A80
Maiolino, R., Shemmer, O., Imanishi, M., et al. 2007, A&A, 468, 979
Marconi, A., Risaliti, G., Gilli, R., et al. 2004, MNRAS, 351, 169
Merloni, A., Bongiorno, A., Brusa, M., et al. 2014, MNRAS, 437, 3550
Mor, R., & Netzer, H. 2012, MNRAS, 420, 526
Mor, R., & Trakhtenbrot, B. 2011, ApJL, 737, L36
Mullaney, J. R., Alexander, D. M., Goulding, A. D., & Hickox, R. C. 2011, MNRAS, 414, 1082
Mullaney, J. R., Daddi, E., Béthermin, M., et al. 2012, ApJL, 753, L30
Neistein, E., & Netzer, H. 2014, MNRAS, 437, 3373
Nenkova, M., Sirocky, M. M., Ivezić, V., & Elitzur, M. 2008a, ApJ, 685, 147
Nenkova, M., Sirocky, M. M., Nikutta, R., Ivezić, V., & Elitzur, M. 2008b, ApJ, 685, 160
Netzer, H. 2009, MNRAS, 399, 1907
Netzer, H. 2013, The Physics and Evolution of Active Galactic Nuclei (Cambridge: Cambridge Univ. Press)
Netzer, H. 2015, ARA&A, 53, 365
Netzer, H., & Laor, A. 1993, ApJL, 404, L51
Netzer, H., Lira, P., Trakhtenbrot, B., Shemmer, O., & Cury, I. 2007, ApJ, 671, 1256

Netzer, H., Mor, R., Trakhtenbrot, B., Shemmer, O., & Lira, P. 2014, ApJ, 791, 34
Nguyen, H. T., Schulz, B., Levenson, L., et al. 2010, A&A, 518, L5
Nordon, R., Lutz, D., Genzel, R., et al. 2012, ApJ, 745, 182
Oh, K., Yi, S. K., Schawinski, K., et al. 2015, ApJS, 219, 1
Oliver, S. J., Bock, J., Altieri, B., et al. 2012, MNRAS, 424, 1614
Page, M. J., Symeonidis, M., Vieira, J. D., et al. 2012, Natur, 485, 213
Pascale, E., Auld, R., Dariush, A., et al. 2011, MNRAS, 415, 911
Pilbratt, G. L., Riedinger, J. R., Passvogel, T., et al. 2010, A&A, 518, L1
Polletta, M., Tajer, M., Maraschi, L., et al. 2007, ApJ, 663, 81
Polletta, M. d. C., Wilkes, B. J., Siana, B., et al. 2006, ApJ, 642, 673
Ricci, C., Paltani, S., Awaki, H., et al. 2013, A&A, 553, A29
Richards, G. T., Lacy, M., Storrie-Lombardi, L. J., et al. 2006, ApJS, 166, 470
Rigby, E. E., Maddox, S. J., Dunne, L., et al. 2011, MNRAS, 415, 2336
Rodighiero, G., Daddi, E., Baronchelli, I., et al. 2011, ApJL, 739, L40
Rosario, D. J., Santini, D. J., Lutz, P., et al. 2012, A&A, 545, A45
Rosario, D. J., Santini, P., Lutz, D., et al. 2013, ApJ, 771, 63
Roseboom, I. G., Lawrence, A., Elvis, M., et al. 2013, MNRAS, 429, 1494
Rowan-Robinson, M., Oliver, S., Efstathiou, A., et al. 1999, ESA Special Publication 427, The Universe as Seen by ISO, ed. P. Cox, & M. Kessler (Tvoordwijk: ESA), 1011
Runnoe, J. C., Brotherton, M. S., & Shang, Z. 2012a, MNRAS, 422, 478
Runnoe, J. C., Brotherton, M. S., & Shang, Z. 2012b, MNRAS, 426, 2677
Santini, P., Rosario, D. J., Shao, L., et al. 2012, A&A, 540, A109
Savage, R. S., & Oliver, S. 2007, ApJ, 661, 1339
Schreiber, C., Pannella, M., Elbaz, D., et al. 2015, A&A, 575, A74
Scoville, N., Aussel, H., Brusa, M., et al. 2007, ApJS, 172, 1
Shao, L., Lutz, D., Nordon, R., et al. 2010, A&A, 518, 4
Shemmer, O., Netzer, H., Maiolino, R., et al. 2004, ApJ, 614, 547
Shen, Y., Richards, G. T., Strauss, M. A., et al. 2011, ApJS, 194, 45
Silverman, J. D., Lamareille, F., Maier, C., et al. 2008, ApJ, 696, 17
Simpson, C. 2005, MNRAS, 360, 565
Speagle, J. S., Steinhardt, C. L., Capak, P. L., & Silverman, J. D. 2014, ApJS, 214, 15
Stalevski, M., Fritz, J., Baes, M., Nakos, T., & Popović, L. Č. 2012, MNRAS, 420, 2756
Stanley, F., Harrison, C. M., Alexander, D. M., et al. 2015, MNRAS, 453, 591
Steffen, A. T., Barger, A. J., Cowie, L. L., Mushotzky, R. F., & Yang, Y. 2003, ApJL, 596, L23
Thacker, R. J., MacMackin, C., Wurster, J., & Hobbs, A. 2014, MNRAS, 443, 1125
Trakhtenbrot, B., & Netzer, H. 2012, MNRAS, 427, 3081
Treister, E., Krolik, J. H., & Dullemond, C. 2008, ApJ, 679, 140
Tsai, C.-W., Eisenhardt, P. R. M., Wu, J., et al. 2015, ApJ, 805, 90
Ueda, Y., Akiyama, M., Hasinger, G., Miyaji, T., & Watson, M. G. 2014, ApJ, 786, 104
Vardanyan, V., Weedman, D., & Sargsyan, L. 2014, ApJ, 790, 88
Vestergaard, M., & Osmer, P. S. 2009, ApJ, 699, 800
Viero, M. P., Asboth, V., Roseboom, I. G., et al. 2014, ApJS, 210, 22
Vito, F., Gilli, R., Vignali, C., et al. 2014, MNRAS, 445, 3557
Volonteri, M., Capelo, P. R., Netzer, H., et al. 2015a, MNRAS, 452, L6
Volonteri, M., Capelo, P. R., Netzer, H., et al. 2015b, MNRAS, 449, 1470
Wang, J.-M., Qiu, J., Du, P., & Ho, L. C. 2014, ApJ, 797, 65
Weedman, D., Sargsyan, L., Lebouteiller, V., Houck, J., & Barry, D. 2012, ApJ, 761, 184
Wright, E. L., Eisenhardt, P. R. M., Mainzer, A. K., et al. 2010, AJ, 140, 1868
Wuyts, S., Förster Schreiber, N. M., Lutz, D., et al. 2011, ApJ, 738, 106
Yaqoob, T., Murphy, K. D., Miller, L., & Turner, T. J. 2010, MNRAS, 401, 411